Three-dimensional electron microscopy of biological macromolecules

B. K. Vaĭnshteĭn
Institute of Crystallography, USSR Academy of Sciences
Usp. Fiz. Nauk **109**, 455-497 (March 1973)

The problem is treated of reconstructing the spatial structure of biological macromolecules and their aggregates (e.g., in viruses and crystals) from electron micrographs, which are two-dimensional projections of these three-dimensional objects. Potentialities of the physical methods (optical diffraction, filtering, and holography) in interpreting electron micrographs are described. The fundamentals are given of the mathematical theory of three-dimensional reconstruction from projections: the Fourier method, the algebraic methods, and the analytical methods. Applications are reviewed of the three-dimensional reconstruction methods in studying a number of objects: protein crystals, helical structures made of globular proteins, bacteriophages, and spherical viruses.

TABLE OF CONTENTS

1. INTRODUCTION

Electron microscopy has been one of the few methods whose emergence has permitted a qualitative leap in the development of the sciences of the microstructure of matter. This is especially true of biology. The latter, in going beyond the level of optical microscopy (observing cells and large microorganisms), has gained the ability to observe structure at resolutions down to ~ 10 Å, i.e., structural details of organelles of cells and viruses, and finally, in recent years, to proceed to studying the structures of individual biological macromolecules (biomolecules). The latter topic will be the specific subject of our discussion, not merely in the aspect of observing these molecules, but in getting data on their three-dimensional spatial structure as based on electron micrographs.

a) Potentialities of the electron-microscope method. The resolution of the best modern commercial electron microscopes is as good as 2—3 Å, which is near the theoretical limit (1.5 Å for 100 kV).[1-3] However, unfortunately, this resolution cannot be realized at present as applied to biomolecules. The problem is that they are made of the light atoms C, N, O, and H, which weakly scatter and absorb electrons. Thus the contrast proves to be insufficient in the electron images of these molecules themselves, or of the molecules as compared with the substrate (carbon or organic films). Hence, people resort to methods of so-called staining,[4-7] by introducing into the specimen substances that strongly scatter electrons, e.g., uranyl acetate, phosphotungstic acid, etc. In positive staining (Fig. 1a), one covers, or wraps, the surfaces of the biomolecules or some of their aggregates with a thin layer of such a material. The method of negative staining (Fig. 1b) is more customary. Here the specimen is immersed in a mass of stain. The latter forms a mold of the object. The stain also penetrates into the cavities of the studied object, e.g., in studying protein crystals, it replaces the mother liquor that lies between the biomolecules or their subunits in such a crystal (Fig. 1c, d). Naturally, when electrons are transmitted through a stained specimen, the obtained pattern arises mainly from the distribution of the stain, which in some way reflects the structure of the scattering object.

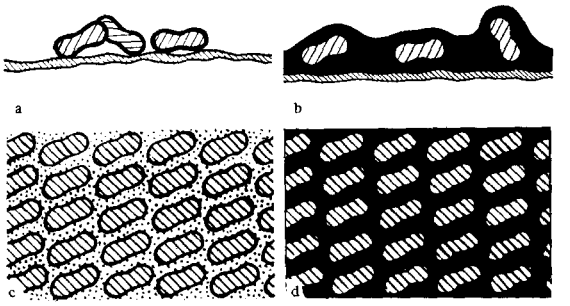

FIG. 1. Positive (a) and negative (b) staining of biomolecules on a substrate (the stain is the dark area); diagram of the structure of a protein crystal: molecules and mother liquor between them (c); a negatively stained protein crystal (d).

The stain distribution always shows certain inhomogeneities. On the other hand, biomolecules and their aggregates (e.g., viruses, ribosomes, and protein crystals) possess very complex structures, which at the same time are maintained by relatively weak forces. Hence, the stain can affect them severely, and their structure and shape can undergo certain changes. All of this reduces the actually attainable resolution in staining of biomolecules to 30—20 Å, and in the better studies, to 15—10 Å.

Another fundamental restriction of the electron-microscope image is that it is only an enlarged shadow, or projection, of the object. Owing to the small aperture ($\sim 10^{-2}$ radian), the depth of focus of the electron microscope amounts to about 2000 Å, which approximately matches the thicknesses of the studied objects, or exceeds them. The intensity of the electrons transmitted through the object is determined by the distribution of matter in it, i.e., by the corresponding absorption (and scattering) $\mu(x, y, z)$ for the penetrating radiation

($\mu = 1 - Q$, where Q is the total effective scattering cross-section):

$$I(x, z) \sim I_0 \exp\left[\int \mu(x, y, z)\, dy\right], \quad D(x, z) = f[I(x, z)], \quad (1)$$

where D is the blackening. The blackening law is usually logarithmic. Thus, if we know the absorption coefficients for electrons, μ_s in the stain and μ_p in the protein (the former plays the major role, as the values of μ_p are negligibly small in comparison with μ_s), we can transform from the observed blackening on the photographic plate to relative or absolute values of the projected matter distribution in the object (see below). However, we do not have direct information on the three-dimensional structure.

In spite of these limitations (in resolution and in planarity of the image), electron microscopy of biological specimens has brought a number of remarkable advances in the fundamentals of molecular biology. Among them are the discovery of the symmetrical structure of spherical and cylindrical viruses, the molecular structure of muscle and its protein components, the study of the structures of ribosomes and mitochondria, and the structure of a number of individual biomolecules, etc.

What do these studies provide, and what level of organization of biomolecules is accessible to electron microscopy? We recall that almost all these molecules are polymeric.[8-10] The chemical formula of the sequence of links in a biopolymer is called the primary structure. This is the topological invariant of the multitude of possible spatial configurations. Some particular stable conformation of certain regions of the chain, e.g., the α helix or the extended β structure in proteins, or the double helix in DNA, is called the secondary structure. The tertiary structure is the concrete conformation of the given biopolymer, e.g., the spatial structure of a polypeptide chain as packed in the compact globule of some protein. The molecules of many proteins consist of several (two, four, or a larger number) of so-called subunits, each of which is an individual coiled polypeptide chain. The spatial combination of subunits into the complex molecule is called the quaternary structure. The information on the secondary and tertiary structures, which requires atomic resolution, comes from X-ray diffraction analysis. However, it is extremely laborious, and applicable to molecules whose number of atoms does not exceed $\sim 10^4$, and is possible only when the object can be crystallized (see, e.g.[9,10]).

The current field of electron microscopy of biomolecules is mainly in studying quaternary structure, and in individual cases, in getting certain crude data on tertiary and secondary structures. At the same time, it is the field of study of combination of molecules of proteins, nucleic acids, and nucleoproteins into aggregates: native ones, such as the viruses, ribosomes, chromosomes, or membranes, or synthetic ones, such as planar monomolecular films, tubes, or crystals. We can call this level of organization the fifth-order level, or quinary structure. The number of atoms combined into a quaternary or quinary structure is of the order of 10^5–10^7. Of course, they cannot be observed individually. However, we can get direct information on the dimensions, shape, and mutual arrangement of the molecules made of these atoms, and on conformational changes in the quaternary structure when such occur, etc.

Thus, both in the attainable resolution and in the level of organization of biosystems, electron microscopy extends the "atomic" level of x-ray diffraction analysis toward larger objects of study. Other physical methods that give additional information at about the same level (on the molecular weight, mean dimensions of macromolecules, etc.) are small-angle x-ray scattering, sedimentation analysis (centrifugation), viscometry, etc. It is always desirable to account for data obtained from them, because the natural state of biomolecules is in solution or in a hydrated medium, whereas mounting of specimens often results in desiccating them in vacuo, and the study itself is conducted in vacuo,[4,5] although there are treatments that permit one to avoid this situation (see, e.g.[3]).

b) Interpretation of electron micrographs. Figures 2–10 show electron micrographs of some biological objects.[11-25] In most cases, the investigators have restricted themselves to measuring the dimensions of the studied object and describing it qualitatively. In a number of cases, especially when several views have been taken, i.e., projections of the object, the researcher's spatial imagination and intuition permit him to build an idealized model of the object. Moreover, this is simplified in cases, as are highly typical of biomolecules and their aggregates, when the structure possesses some particular symmetry. Thus, Fig. 2 demonstrates the structure of the glutamate dehydrogenase molecule, which has the symmetry 32,[11] while Fig. 3 shows the structure of the complex molecule of hemocyanin (a blue protein containing copper that transports oxygen in

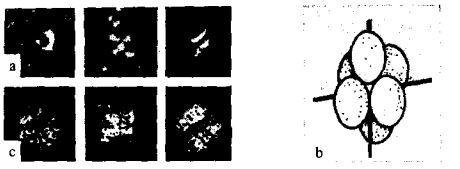

FIG. 2. The glutamate dehydrogenase molecule in different orientations on the substrate: a) (500,000 × magnification); b) the model; c) simulation of projections of the model in the same orientations as calculated by a computer.

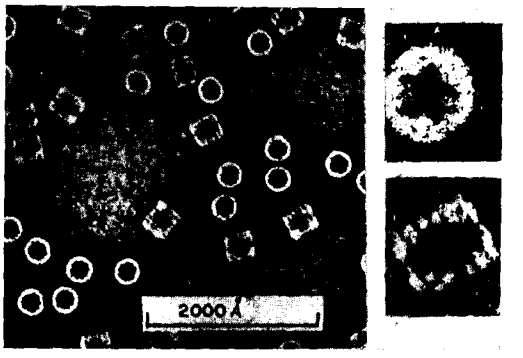

FIG. 3. Molecules of hemocyanin.

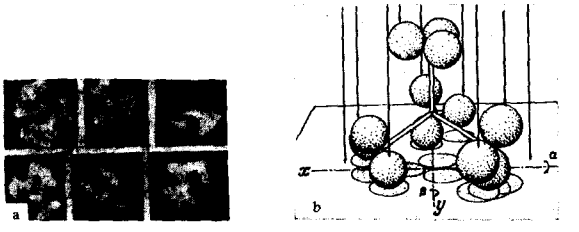

FIG. 4. The glutamate dehydrogenase complex in different projections (1.3×10^6 × magnification) (a); and a model of it (b).

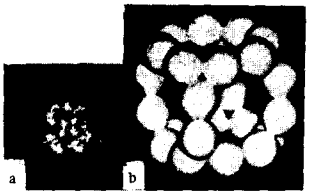

FIG. 5. The pyruvate dehydrogenase complex (a); and a model of it made of 24 subunits (b) (magnification of the model is 8×10^6).

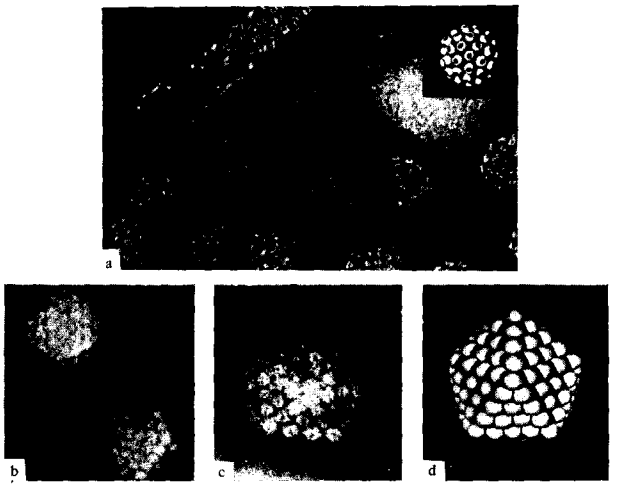

FIG. 6. "Spherical" (icosahedral) viruses: human wart virus and a ball model of it made of 72 units (200,000 X magnification) (a); adenovirus (252 units; 200,000 X magnification) (b); herpes virus (162 units; 220,000 X magnification (c); and a model of it (d).

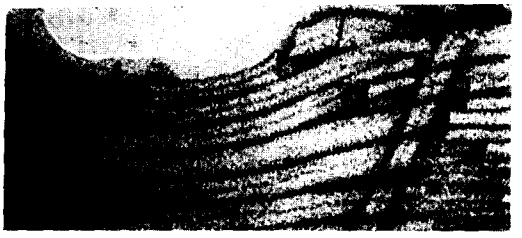

FIG. 7. Tobacco mosaic virus (380,000 X magnification).

mollusks, and has a molecular weight of 8.6 million.)[12] Figure 4 shows pictures that permit one to determine the quaternary structure of the glutamate dehydrogenase complex,[13] and Fig. 5 shows the pyruvate dehydrogenase complex.[14] Figure 6 shows some spherical viruses (human wart virus, herpes virus, and adenovirus)[7,15,16,17] which have icosahedral symmetry (see p. 200 below). Figure 7 is tobacco mosaic virus (TMV),[4,7,17,18] which has helical symmetry. Figure 8 shows the same symmetry in the tails of bacteriophage, and the polyhedral structure of their heads.[4,6,7,19,20] We shall present idealized models of some of these structures.

The problem is more complex when the object is asymmetric. A typical example is ribosomal particles[4,21-23] (see Fig. 9). Evidently, although building of such models is useful, and it gives an understanding of some of the features of the structure of the object, it is not free from the subjective approach.

Great potentialities are opened up by studying symmetrical aggregates of protein molecules obtained in vitro. Figure 10 gives an example. Devising an image-formation model is a definite forward step. For example, one

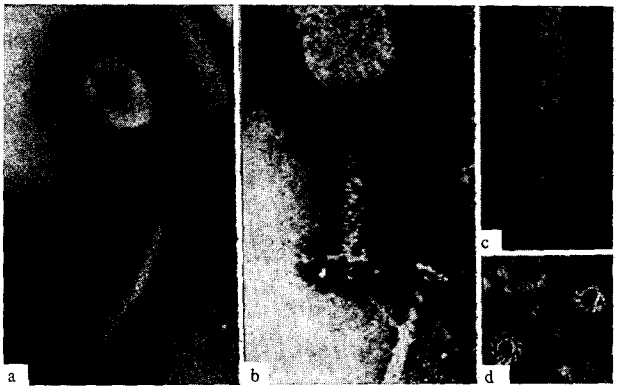

FIG. 8. Bacteriophages of Bacillus mic. (220,000 X magnification) (a); and T4 (300,000 X magnification) (b); unwinding of its tail (c); and an element of the tail (d).

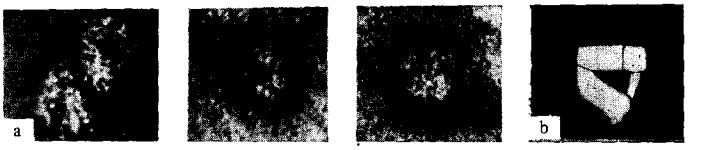

FIG. 9. Ribosomes in different orientations (a) and a diagram of their structure made of subparticles with a canal between them (b) (500,000 X magnification).

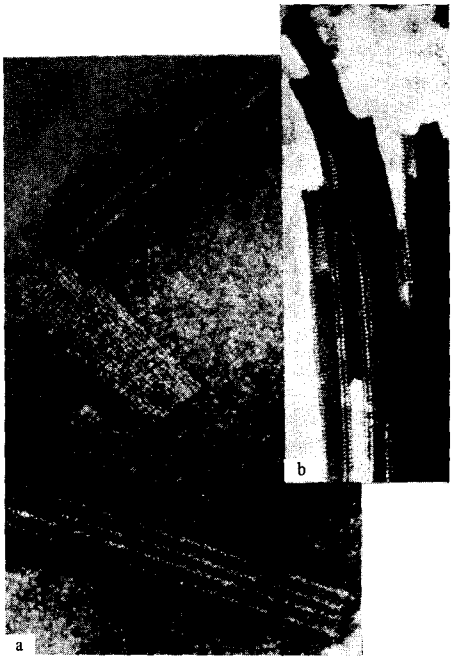

FIG. 10. Monomolecular layers (two-dimensional crystals), tubes, and individual molecules of beef liver catalase (150,000 X magnification) (a); and tubes of human erythrocyte catalase (120,000 X magnification) (b).

can consider the "shadow" of the model of some structure in different orientations (see Fig. 4) by comparing the obtained patterns with electron micrographs. This work can also be relegated to the computer. Figure 11 shows different projections of a polyoma-type virus (such as the human wart virus (see Fig. 6a), which is made of 72 morphological units), as calculated by a computer and as they appear on the screen.[24] These projections imitate the corresponding photographs well. A projection of the glutamate dehydrogenase molecule has also been obtained (see Fig. 2c).

Analysis of the structure of molecules is simplified if they form regular symmetric structures in vitro. For

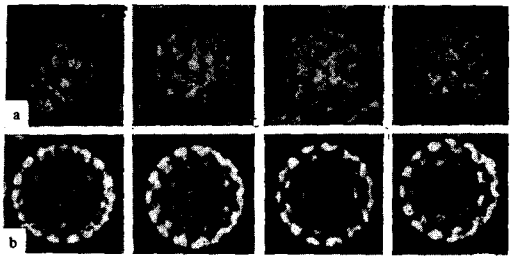

FIG. 11. A polyoma-type virus made of 72 morphological units (a) and a simulation of it in matching orientations as obtained by a computer (b).

example, the protein catalase can form two-dimensional monomolecular layers. Tubular, cylindrical protein crystals (see Fig. 10) were also first discovered with this material.[25-27] Just like a number of other proteins, catalase can also crystallize in a three-dimensional crystal (see Fig. 28 below).

Studies have been conducted in the last five years in the Laboratory of Molecular Biology in Cambridge, in the Institute of Crystallography of the USSR Academy of Sciences in Moscow, and at other places, that permit one to solve quantitatively the problem of determining the three-dimensional structures of objects from their electron micrographs. The main topic of our review is to discuss them. Further, we shall first take up the beautiful physical method of "optical filtering," which gives some information on three-dimensional structure.

2. OPTICAL DIFRACTION, FILTERING, AND HOLOGRAPHY

As I have stated, biological objects in a number of cases are symmetrical. These include two-dimensional crystals (layers) and three-dimensional protein crystals. They include the rodlike viruses and phage tails, which are periodic in one direction, and which possess helical-cylindrical symmetry (see Figs. 7, 8, 10). The "cylindrical crystals" of globular proteins, which are tubes with monomolecular walls (or more rarely, with thicknesses of two or more molecules), have the same symmetry.[25-28] One can get an optical diffraction pattern by shining a beam of coherent (laser) light through an electron micrograph of such an object.[29-31] Figure 12a shows a diagram of an optical diffractometer, which in essence is an Abbe microscope system. The diffraction pattern is determined by the Fourier integral of the optical density D(x, y) of the micrograph:

$$\Phi(X, Y) = \int D(x, y) \exp[2\pi i (xX + yY)]\, dx\, dy = \mathfrak{F}[D]. \quad (2a)$$

One can observe this pattern (with an intensity $I \sim |\Phi|^2$) in the back focal plane of the diffractometer. In the general case, the value of Φ is distributed continuously in this plane. The optical density is a superposition of the image D_p of the periodic structure and the background noise D_b:

$$D = D_p + D_b. \quad (3)$$

The background includes the image of the substrate and deviations from periodicity in the object itself. The diffraction from the periodic component

$$\mathfrak{F}[D_p] = \int D_p(x, y) \exp[2\pi i (hx + ky)]\, dx\, dy = \Phi_{hk} = |\Phi_{hk}| e^{i\alpha_{hk}} \quad (2b)$$

is concentrated at the lattice sites hk of the reciprocal lattice of the object which have the coordinates x = h/a and y = k/b (a and b are the periods). Figure 12b gives as an example an electron micrograph of a monomolecular layer of a "two-dimensional crystal" of the protein phosphorylase b,[28] and Fig. 12c gives the optical diffraction pattern of this layer. If we collect the diffracted beams of (2a) with a lens, which corresponds to the inverse Fourier transform

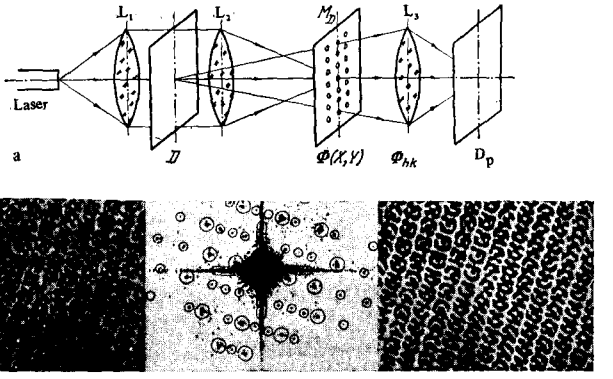

FIG. 12. a) Diagram of an optical diffractometer (L_1–L_3 are the lenses of the optical system, D is the object (an electron micrograph), M_D is the diffraction plane and a mask that transmits only the Φ_{hk}, D_p is the plane of the (filtered) image); b) an electron micrograph of a crystalline layer of the protein phosphorylase b; c) its diffraction pattern (the circles correspond to the holes in the mask that transmit only the Φ_{hk} diffraction from the periodic component of the image); d) the filtered image.

$$\mathfrak{F}^{-1}[\Phi(X, Y)] = D(x, y), \quad (4)$$

then we get again an image of the micrograph. However, we can use the fact that the diffracted beams Φ_{hk} from the periodic component D_p are spatially isolated, by placing in the diffraction plane a screen with apertures (a mask) having coordinates corresponding to the lattice points of the reciprocal lattice. That is, we can perform optical filtering[32] (Fig. 12d). The mask is prepared to fit the diffraction pattern. Then the image will give only the contribution of the component (2b), and as in any optical instrument, the transmitted Φ_{hk} will keep their own phases. (They would have been lost if a photograph had been taken in the diffraction plane, since a photographic plate records $I \sim |\Phi|^2$.) However, the diffracted beams $\mathfrak{F}[D_b]$ will be stopped. Thus we get a cleaned-up (filtered) picture of the periodic structure alone:

$$\mathfrak{F}^{-1}[\Phi_{hk}] = D_p(x, y). \quad (5)$$

In addition to the problem of refining the image, optical diffractometry permits one to determine the lattice periods very exactly.

However, the most elegant application of this method, which reveals the structure of the object in the third dimension, is diffraction from helical cylindrical structures like the cylindrical viruses, phage tails, and monomolecular tubes. These objects show periodicity along the principal axis (with period c), and their symmetry is most often described by groups of the type $s_{p/q}N$.[33-36] Here $s_{p/q}$ is the operation of screw translation by the angle $\alpha = 2\pi q/p$ (which amounts to one pth of q complete turns) with simultaneous translation along the axis by c/p. In addition to this symmetry operation, which relates packing units of the helical structure (e.g., protein molecules) to one another, these structures often also have a simple rotation axis of order N (usually N = 2, 3,

6, ...) that determines the "strandedness" of the helix. The diffraction from such structures having the period c and the scattering density $\rho(r, \psi, z)$ is determined by the Fourier-Bessel transform[33-36]

$$\Phi(R, \Psi, Z) = \sum_{n=-\infty}^{+\infty} \exp\left[in\left(\Psi + \frac{\pi}{2}\right)\right] \int_0^{\infty} \int_0^{2\pi} \int_0^{c} \rho(r, \psi, z) \times J_n(2\pi rR) \exp\{-i(n\psi + 2\pi zZ)\} r\, dr\, d\psi\, dz. \quad (6)$$

The electron micrograph is a projection of the structure $\rho(r, \psi, z)$.

According to the general properties of transforms (see below, (21), (22)), the diffraction from a projection is determined by the cross-section of the transform (6) at a certain value of Ψ. The analog of the reciprocal lattice of a crystal here is the so-called cylindrical reciprocal lattice, whose maxima correspond to the maxima of the Bessel functions J_n entering into Eq. (6). The latter are determined by the selection rule

$$l = mp + (nq/N), \quad (7)$$

Here q and p are the symmetry parameters of the helix, l is the number of the layer line in the diffraction pattern, such that $Z = l/c$; $m = 0, \pm 1, \pm 2$, etc. Figures 13 and 14 give examples of optical diffraction from this type of structures. Figure 13 illustrates the diffraction pattern of the monomolecular tube of catalase in Fig. 10a. Its parameters are c = 540 Å, p/q = 70/11, and N = 1. The outer diameter of the tube is 290 Å.[37] Phosphorylase b forms analogous tubes, as in Fig. 14a (molecular weight = 350,000, c = 840 Å, p/q = 27/7, N = 4, and d = 320 Å).[28] Figure 14b shows the optical diffraction pattern, with the coordinate grid of a plane section of the cylindrical reciprocal lattice drawn on it. It is important to note that this plane section actually breaks down into two nets (which are provisionally denoted in Figs. 13—14b with one in solid lines, and the other in dotted lines). One of them corresponds to diffraction from the "front" wall, and the other from the "back" wall of the tube made of helically packed molecules.

This circumstance allows us to use the idea of optical filtering by preparing a mask with holes corresponding to one of the nets (see Fig. 14c). The slits in the mask are elongated to fit the profile of the diffraction maxima, which are determined by the radial spread of the peaks of the Bessel functions J_n. The zero-order peak is attenuated with a filter to half-intensity. The obtained image (Fig. 14d) is thus one side of the tube; the background has also been filtered out of it. The mirror-equivalent mask (see Fig. 14c) transmits the diffracted beams from the other side of the tube, and correspondingly gives its image (see Fig. 14e). We can distinctly see the helical packing in these images, and the structure of the individual protein molecules that form the

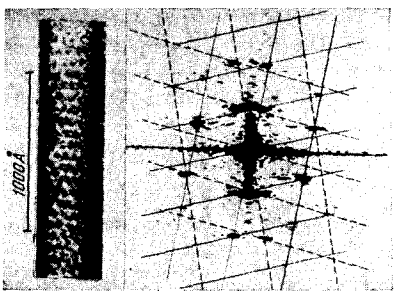

FIG. 13. A catalase tube and its optical diffraction pattern (cf. Fig. 10a).

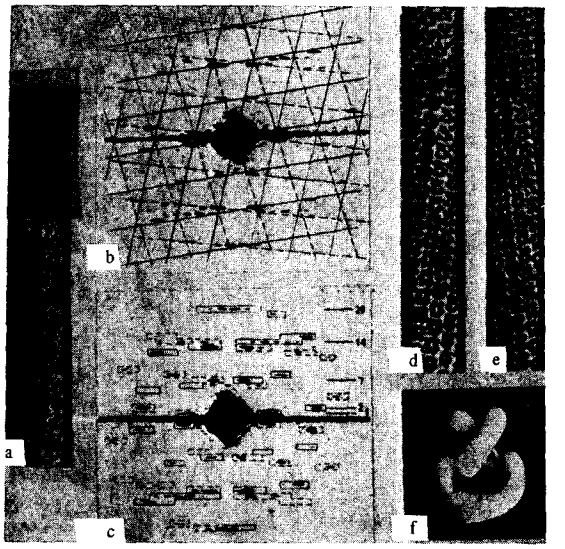

FIG. 14. Electron micrograph of a tube made of phosphorylase b (a); its optical diffraction pattern with two families of diffraction spots corresponding to the front and back walls of the tube (b); the same pattern with the slits of the two corresponding masks (c); the filtered image of the front and back sides of the tube (d and e); and a model of the molecule (f).

packing is already manifested. Their appearance in different angular orientations in the tube made it possible to build a model of the molecule: it is made of four bent subunits arranged at the vertices of a tetrahedron (see Fig. 14f). A number of other objects having helical symmetry have been studied in the same way. Thus, a step has been taken out of the plane of the electron-optical picture into the third dimension of the studied objects by using this optical method (with visible light rays).

All of the optical procedure of filtering from noise, or isolating part of an image, can be replaced by computer calculation by the formulas (2)—(7) described above. The source material for this is the measurement of the optical density D of the micrograph. This method is more complex, but it gives precise quantitative results. Here one can also avoid difficulties in interpreting the secondary (filtered) image that involve photographic methodology (accounting for the light curves of blackening, etc.). In this procedure, the moduli $|\Phi_{hk}|$ and their phases α_{hk} must enter in calculating Eq. (5).

One can take another path: to combine optical and computing methods by using the principles of holography.[38] As we know, in order to do this, one mixes in the plane of the hologram the radiation coherently scattered by the object with a reference beam coherent with it. The interference pattern, or hologram, contains a record of the phases, and it reproduces an image of the object when illuminated with coherent light. In holography of aperiodic objects, one does not measure the hologram itself, and one cannot in practice determine the phases corresponding to each of its points. However, the hologram of a periodic object obtained near the diffraction plane permits one to determine the phases of the spots hk. We shall call such a hologram a "phasogram". Figure 15a shows a region of a micrograph of a two-dimensional monomolecular layer of catalase. Figure 15b shows the phasogram, and Fig. 15c shows its magnified reflections. We see that each spot is crossed by interference fringes. Superposition of the reference wave $\Phi_0 = e^{i\omega x}$ ($\omega = (2\pi/\lambda) \sin \varphi$, where φ is the angle of inci-

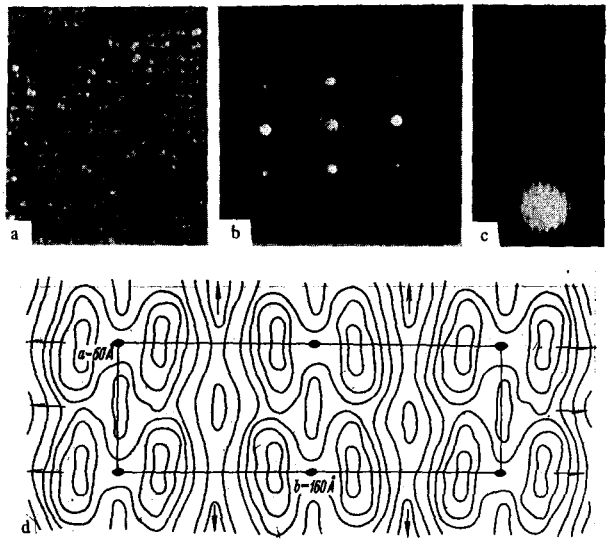

FIG. 15. A monomolecular layer of catalase (a); its phasogram (b); a magnified image of the reflections (c); and an image of the molecules calculated from intensities and phases found from b and c (d).

dence on the photographic plate) and Φ_{hk} will give[39]

$$I_{av} \sim (1/2) + (1/2) \mid \Phi_{hk} \mid^2 + \mid \Phi_{hk} \mid \cos(\alpha - \omega X). \qquad (8)$$

Measurement of the amount of shift of the interference fringes in the spots $\Delta X = \Delta\alpha/\omega = \lambda/2 \sin\varphi$ determines the relative phases α in (2b), and $|\Phi_{hk}| = I_{hk}^{1/2}$. We can now calculate a Fourier synthesis by Eq. (5) using these quantities. This is shown in Fig. 15c as a contour plot. Thus we get here a quantitative description of the periodic component of the image (Fig. 15a).

Of course, one can also reconstruct the image optically from the hologram,[38] and if one combines the phasogram principle with the principle[32] of filtering one of the components of the image (by superposing a mask on it), then one should reconstruct one such component such as Fig. 14c, d.

In line with our treatment here of problems of optical diffraction and holography, with application thus far to the light-optical interpretation of electron-optical images, it is pertinent to mention the possibilities of applying these same ideas in electron optics itself. In principle, of course, all of this can be achieved for electron waves as well. However, in practice, it has not yet been possible to invent analogous electron-optical systems having the necessary minimum of their numerous inherent aberrations. While electron diffraction from crystals became a working method of structure analysis long ago,[39] it is a complex problem to get diffraction patterns from proteins, as the patterns are concentrated at very small angles because of the huge interplanar distances. It can be solved by using electron-optical systems that magnify the deflection angles of the diffracted beams, i.e., as though increasing the effective length of the instrument. Figure 16 gives an example of diffraction from the same catalase specimen as a whole in the electron microscope.[40]

In their origin, the ideas of holography have been aiming in many ways at electron microscopy.[3,41-43] The problem hinges on a coherent source of electrons. Moreover, one still can't avoid using magnifying electron optics with its aberrations, since the hologram must be recorded on a photographic plate having a resolving power comparable with that needed for electron waves

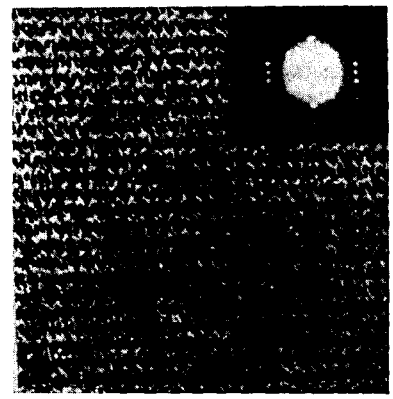

FIG. 16. A three-dimensional crystal of orthorhombic catalase and its corresponding electron-diffraction pattern.

having $\lambda \sim 0.05$ Å. Nevertheless, current estimates show that one can hope to increase the resolution (for non-biological specimens) to ~0.4 Å by using the holographic principle.[3] The image can be reconstructed from the hologram by the optical-analog method or by computer calculation.[3,44,45] However, there are as yet no actual studies on any concrete objects, including biological.

In closing this chapter, we note that, in addition to amplitude contrast in the image, which is due to absorption of electrons in the specimen, electron micrographs of biological specimens can also show the so-called phase contrast. The latter is due to the phase difference upon scattering in the specimen and the substrate, to defocusing, and to spherical aberration. Methods have been developed for accounting for and eliminating this type of distortion.[46-50]

3. THE MATHEMATICAL APPARATUS OF THREE-DIMENSIONAL RECONSTRUCTION

a) The object and its projections. We have already stated that micrographs obtained in transmission electron microscopy, when recalculated appropriately, are two-dimensional projections of the object.

Let $\rho(\mathbf{r})$ be the function describing the structure of the object, i.e., its density distribution. Then $\rho(\mathbf{r})$ can describe an individual macromolecule or a set of them, in shape and relative arrangement, e.g., an association of them in a virus particle or in a crystal structure. In the general case, this function thus describes various continuous or discrete distributions having variable density, and it is defined over a limited region.[51,52]

We shall take ρ to be the distribution of matter in the biomolecule, e.g., a protein. This distribution is a "negative" of the overall distribution of scattering density in the specimen, which consists of protein and stain. Thus, $\rho(\mathbf{r}) > 0$.[1)] Since the stain does not penetrate the protein, then we can use a function $\rho^c(\mathbf{r})$ of a special type to describe stained specimens. It is equal to unity within the boundary surface $S(\mathbf{r})$ of the protein, and zero outside (Fig. 17):

$$\rho^c(\mathbf{r}) = \begin{cases} 1 \text{ within } S(\mathbf{r}), \\ 0 \text{ outside } S(\mathbf{r}). \end{cases} \qquad (9)$$

$S(\mathbf{r})$ also describes internal surfaces if they exist.

The projection of $\rho(\mathbf{r})$ along some direction y, onto the line x perpendicular to y in the two-dimensional case, or onto the plane $\mathbf{x}$ in the three-dimensional case, is defined by the formula

$$L(\mathbf{x}) = \int \rho(\mathbf{r})\, dy. \qquad (10)$$

The function $L(\mathbf{x})$ is a very simple integral representation of the function $\rho(\mathbf{r})$.(see Fig. 17). If we continuously vary the direction y of projection, we get a continuous set of $L(\mathbf{x})$; $\rho(\mathbf{r})$ unambiguously defines the set of $L(\mathbf{x})$. Evidently the converse is true: the set of $L(\mathbf{x})$ defines the original function $\rho(\mathbf{r})$. The three-dimensional problem is reduced to a two-dimensional problem if all the directions of projection y_i are coplanar, e.g., all perpendicular to z. Such projections can be called coaxial (Fig. 18a). In them, the two-dimensional cross-sections of the function $\rho(x, y, z)$ project into the one-dimensional functions $L^{i,k}(x_i, z_c)$, and the three-dimensional problem is reduced to a set of two-dimensional problems for $z_c = \text{const}$.

For the two-dimensional case, if (x_ψ, y_ψ) is a coordinate system rotated through the angle ψ with respect to $\mathbf{r}(x, y)$, the projection along the line y_ψ has the form

$$L(\psi, x_\psi) = \int \rho(\mathbf{r})\, dy_\psi \qquad (11)$$

and ψ is a variable parameter that determines $L(x_\psi)$ (Fig. 18b).

The continuous set of projections $L(\psi, x_\psi)$ of the object $\rho(\mathbf{r})$ can be called its projection transform. Figure 19 shows a two-dimensional asymmetric object, or

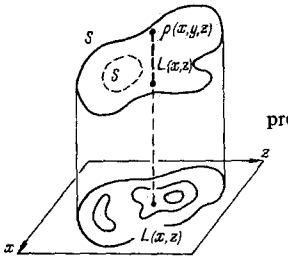

FIG. 17. The function $\rho(x, y, z)$ and its projection $L(x, z)$.

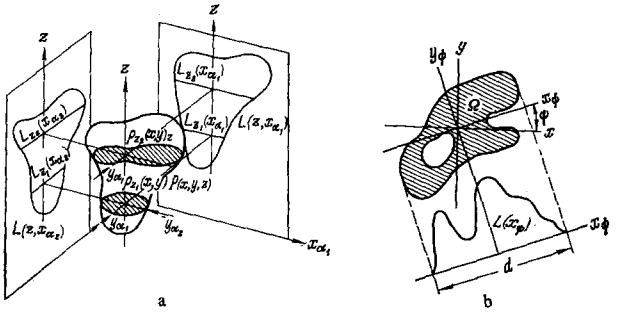

FIG. 18. Coaxial projection (a) and a one-dimensional projection $L(x_\psi)$ of a two-dimensional function (b).

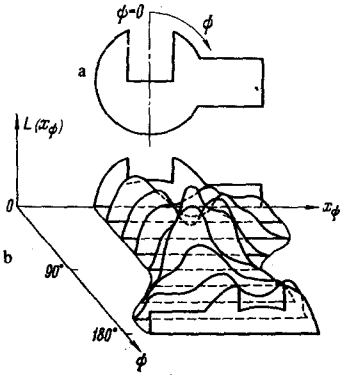

FIG. 19. A wrench (a) and its projection transform (b).

"wrench," and its projection transform as represented as a set of "cross-sections" having $\Delta\psi = \pi/8 = 22.5°$.

Thus our problem can be formulated as follows: to reconstruct the structure $\rho(\mathbf{r})$ from the projection transform $L(\psi, z_\psi)$, or in practice, from some set of p projections L^i (i = 1, 2, ..., p). Exactly the same problem has been posed also in (macroscopic) radiography (röntgenoscopy),[53-55] and analogous problems have been solved in radioastronomy[56-58] and in the field of image transfer.[59]

The following normalization condition[52] holds for the function $\rho(\mathbf{r})$ and any of its projections:

$$\Omega = \int \rho(\mathbf{r})\, dv_r = \int L^i(\psi_i, x_i)\, dx_i. \qquad (12)$$

In the approximation $\rho = \rho^c$ of Eq. (9), Ω is nothing other than the volume of the object (or its area in the two-dimensional case, as in Fig. 18b). The volume of the object, e.g., molecules or viruses, is usually known from data on the density or molecular weight. By using (12), we can express the relative values of L obtained from an electron-microscopic experiment in absolute values. Under certain conditions, one can also find the absolute values of L directly from measuring relative blackenings on the photographic plate.[60]

In practice, one reconstructs ρ within a certain volume v (within an area in the two-dimensional case). If the diameter of the function $|\rho| > 0$ is D, then one can perform the reconstruction in an area having a side a $\geq$ D, so that

$$\bar{\rho} = \Omega/a^2, \qquad (13)$$

where $\bar{\rho}$ is the mean.[52]

b) Discretization. The experimentally obtained projections L^i are either measured directly as a set of discrete values $L^i_j(x_{\psi_i})$ at a certain spacing in x_ψ, or they are transformed into the latter for input into a computer. On the other hand, $\rho(\mathbf{r})$ is reconstructed over a certain discrete point set. In this case, if we consider the two-dimensional case, and bear the condition (13) in mind, we shall dissect the square region of side a $\geq$ D into m^2 nodes having weights $\rho_{jl} = \rho(ja/m, la/m)$. (One can also work with a hexagonal grid.) Let us choose the same spacing a/m for the projection. Then, upon oblique projection,

$$L(\psi_i, x_{\psi_i}) \approx L^i_k(ka/m) = \sum{}' \rho_{jl}, \qquad (14a)$$

Here the summation Σ' is taken over the points ρ_{jl} that lie in a strip of width a/m along the axis y_{ψ_i} passing through the point $x_{\psi_i} = ka/m$. We should note that the quantities L^i_k are sensitive to the spacing of the partition grid, and they can deviate from the true L^i of (11) as the spacing is increased.

The normalization conditions (12) and (13) take on the form

$$\Omega = \sum_{j,l} \rho_{jl} = \sum_k L^i_k, \qquad (14b)$$

$$\bar{\rho} = \Omega/m^2. \qquad (14c)$$

For the contrast function ρ^c of (9),

$$\rho^c_{jl} = 0 \text{ или } 1, \qquad (15a)$$

$$\Omega^c = w, \qquad (15b)$$

$$\bar{\rho^c} = w/m^2, \qquad (15c)$$

where w is the number of grid points within the boundary S. Then the sought function (15a) is described simply as a square matrix of ones and zeros.

c) Symmetry properties of projections. One can get information on the three-dimensional structures of asymmetric objects only when one has different projections of the object. They can be recorded if the object rests at random on a substrate in different orientations, but these orientations must be determined. One can get systematic information by photographing an asymmetric object at different inclinations to the beam, or coaxial projection (see Fig. 18a).

It is always true of an asymmetric object that

$$L(\psi,\ x_\psi) = L(\psi + \pi,\ -x_\psi). \tag{16a}$$

That is, projections rotated by the angle π are alike, but they run in opposite directions (see Fig. 19b).

We have stated that many biomolecules and their aggregates are symmetrical. If the object has an N-fold rotation axis, then

$$\begin{gathered}\rho(x,\ y) = \rho(-x,\ -y),\ \text{то} \\ L(\psi,\ x_\psi) = L(\psi,\ -x_\psi),\end{gathered} \tag{16b}$$

while (16a) is simultaneously obeyed, Fig. 20 gives as an example an object with N = 6. The projections along its directions ψ_i differing by $2\pi/6 = 60^\circ$ are identical. We must also bear in mind a property of projections of objects having a twofold axis (N = 2, and in general for symmetry axes of even order N = 2k). Since here $\rho(x, y) = \rho(-x, -y)$, then

$$\begin{gathered}L(\psi, x_\psi) = L(\psi + i(2\pi/N),\ x_{\psi+i(2\pi/N)}) \\ (i = 1,\ 2,\ \ldots,\ N)\end{gathered} \tag{16c}$$

while again (16a) holds simultaneously. In other words, the projections of such objects contain independent information only in the region $(0, x_\psi)$ (see Fig. 20). Upon taking account of (16b) and (16c), we can now say that one projection of a symmetrical object may suffice for reconstruction, since it is equivalent to p = N (for N odd) or p = N/2 (for N even) projections of an asymmetric object. In fact, in such an object the independent asymmetric region occurs in p orientations with respect to the direction of projection. If the object contains a screw axis $s_{p/q}$, then (if we project perpendicular to this axis),

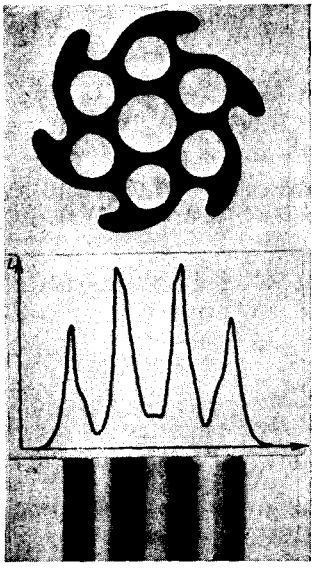

FIG. 20. A figure having the symmetry N = 6 and its projection.

conditions hold that are analogous to (16b) and (16c), but the projections are displaced to different levels in z:

$$\begin{gathered}L(\psi,\ x_\psi,\ z) = L(\psi + i(2\pi/p),\ x_{\psi+i(2\pi/p)},\ z + i(c/p)) \\ (i = 1,\ 2,\ \ldots,\ p)\end{gathered} \tag{16d}$$

If the symmetry group is $s_{p/q}N$, then the order of the group is $\mathcal{N} = pN$, and one projection is equivalent to $\mathcal{N}$ or $\mathcal{N}/2$ (for even $\mathcal{N}$) projections. Thus, the symmetry group is $s_{7/2}/6$ for the T6 phage tail, and one micrograph (see also below, Fig. 49) is equivalent to 21 projections.

Objects like the spherical viruses or individual molecules are described by point groups of symmetry. For example, these viruses have the icosahedral symmetry 532. Their projections along symmetry axes have the corresponding symmetries. Such a projection is equivalent to $\mathcal{N}/\mathcal{N}'$ independent projections, where $\mathcal{N}$ and $\mathcal{N}'$ are the orders of the point group of the object and of its projection, respectively.

d) On methods of reconstruction. The mathematical problem of reconstructing a function from its projections was solved long ago, both from the standpoint of Fourier transforms and directly by operating in **r** space. However, as often happens in modern science, the results of mathematicians and specialists in other fields did not immediately fall in the field of view of electron microscopists, and they developed a number of the methods anew, but at the same time, they introduced some new ideas into the mathematical theory as well.

We must also note the similarity of this problem in a certain aspect to the problem of x-ray structural analysis of crystals or helical structures, where the three-dimensional structure of an object is determined from diffraction data. However, a difference consists in the fact that all the data on the moduli of the structure amplitudes exist in x-ray analysis in reciprocal Fourier space, but there are no data on their phases. Yet here direct images of projections exist, and this means that in reciprocal space data exist both on the moduli and the phases, but not throughout its volume.

e) The algebraic approach. This approach was proposed and carried out in [51,52,61-63] and treated also in [64-68]. It consists in the following. In a discrete representation, the ρ_{jl} are projected into the L^i_k, and (11) is transformed into the linear equations (14a):

$$L^i_k = \sum{}' \rho_{jl} \quad (i = 1,\ 2,\ \ldots,\ p). \tag{17}$$

The number of unknown ρ_{jl} in each equation of (17) is approximately m.

If there are p projections L^i (i = 1, 2, ..., p), then there are pm known L^i_k and m^2 unknown ρ_{jl}. The condition for unique solvability of (17) is:

$$pm \geqslant m^2,\ \text{i.e.},\ p \geqslant m. \tag{18a}$$

The condition (18a) may prove to be excessively rigid. Thus, evidently, when $L^i_j = 0$, all of the $\rho_{jl} = 0$. This gives directly a convex enveloping contour about the outer contour S. The solution is found by inverting the matrix of the linear equations (17).

For contrast functions ρ_c (0, 1), reconstruction algorithms have been developed that work on the principle of sorting.[61-63,67,68] Here the criterion (18a) is sufficient but not necessary, and as estimates have shown, one can get a satisfactory reconstruction when

$$m^c \approx (3-5)\,p. \tag{18b}$$

The conditions (18a) and (18b) define the optimum choice of m, i.e., the cells of the partition grid a/m that give a unique solution. In a certain sense (see p. 196 below), the quantity a/m corresponds to the "resolution" of the reconstructed structure.

The experimental data may prove to be incomplete in that the number p of obtained projections can be small and insufficient for getting the desired partition a/m according to (18a) or (18b). Then the equations (17) become indeterminate. Then one can find all of the solutions by using some algorithm, and select from them certain ones by using additional criteria. We should note that here the sum of any t solutions

$$\sum_{n=1}^{t} \rho_{jl}^{(n)}/t \qquad (19)$$

is also a solution. However, for contrast functions ρ^c_{jl}, such a sum is no longer a contrast function itself, i.e., it does not satisfy the condition (15a). If we use the condition of discrete normalization (15b), we can map the sum of the solutions with a contour line such that w points lie within it. This will be the contour of the most probable solution. The study of catalase was an example of applying the linear-equation method. Figure 21 gives one of the solutions and their sum for one of the cross sections of the three-dimensional crystal (see also Figs. 30b–c below). Thus, the overall pattern of the algebraic methods is:

$$\text{a set of } L^i \to \rho. \qquad (20)$$

f) The double Fourier transformation method.

DeRosier and Klug[64,69,70] proposed this method for three-dimensional reconstruction in electron microscopy (see also[56,57] for the two-dimensional case). In essence it is a mathematical extension of the method of optical filtering. As we know, the Fourier transform of the function $\rho(\mathbf{r})$ and its projection $L(\mathbf{x})$ are related by:

$$\int \rho(\mathbf{r}) \exp(2\pi i \mathbf{r}\mathbf{S})\, dx\, dy\, dz = \mathfrak{F}[\rho] = \Phi(\mathbf{S}). \qquad (21)$$

where $\mathbf{S}(X, Y, Z)$ is the reciprocal-space vector. At the same time,

$$\int L(\mathbf{x}) \exp[2\pi i (\mathbf{x}\mathbf{S}_X)]\, dx\, dz = \mathfrak{F}[L] = \Phi(X, 0, Z) \qquad (22)$$

is the two-dimensional cross section of the transform $\Phi(\mathbf{S})$ in the plane $\mathbf{S}_X$, i.e., for Y = 0. One can reconstruct the functions ρ and L from their transforms by inverse Fourier transformation:

$$\mathfrak{F}^{-1}[\Phi(\mathbf{S})] = \rho(\mathbf{r}), \qquad (23a)$$

$$\mathfrak{F}^{-1}[\Phi(\mathbf{S}_X)] = L(\mathbf{x}). \qquad (23b)$$

Correspondingly, in the two-dimensional case the transform of a projection is a one-dimensional cross section of the two-dimensional transform. If we know several projections, then we can calculate the corresponding cross sections in reciprocal space (Fig. 22), and if there are many of these cross sections, then interpolation between them gives a representation of the structure of the transform $\Phi(\mathbf{S})$, from which we can now transform by (23a) to $\rho(\mathbf{r})$.

Thus, in contrast to (20), the pattern of reconstruction[64] is here:

$$\text{a set of } L^i \to \text{a set of } \mathfrak{F}^i(X_{\Psi_i}) \to \Phi(\mathbf{S}) \to \rho(\mathbf{r}). \qquad (24)$$

The transform (6) of a helical object $\rho(r, \psi, z)$ in cylindrical coordinates can be rewritten in the form

$$\Phi(R, \Psi, Z) = \sum_n G_n(R, Z) \exp[in(\Psi + \pi/2)], \qquad (25a)$$

while the inverse transformation has the form

$$\rho(r, \psi, z) = \sum_n \int g_n(r, Z) \exp(in\Psi) \exp(2\pi i z Z)\, dZ, \qquad (25b)$$

so that g_n and G_n are mutually reciprocal Bessel transforms:

$$G_n(R, Z) = \int_0^\infty g_n(r, Z) J_n(2\pi r R)(2\pi r)\, dr. \qquad (25c)$$

We should note that the selection rule (7) has the effect that each layer line l having $z = l/c$ is practically determined by the one function J_n having the lowest n, with the contribution of the others neglected.

The system of calculation consists in the following.[64,69,70] One calculates from the observed projection L(x, z) a two-dimensional transform like (2a), but it is equivalent to the cross section of the function $\Phi(R, \Psi, Z)$ of (25a) at $\Psi = 0$ and π, so that $X_0 = R_{\Psi=0}$, $-X_0 = X_{\Psi=\pi} = R_{\Psi=\pi}$. The radial component is transformed according to (25c). If the object possesses symmetry, then upon using the conditions (16a)–(16d), one can duplicate this cross section at different angles $\Psi \neq 0$ or π:

$$\Phi(R, 0, Z),\ \Phi(R, \Psi_1, Z),\ \ldots,\ \Phi(R, \Psi_{N-1}, Z). \qquad (26)$$

If one uses a special interpolation procedure between these cross-sections, one gets the three-dimensional transform $\Phi(R, \Psi, Z)$ defined at a sufficient number of points, and its transform by (25b) will give $\rho(r, \psi, z)$. Figure 23 gives as an illustration the values of the

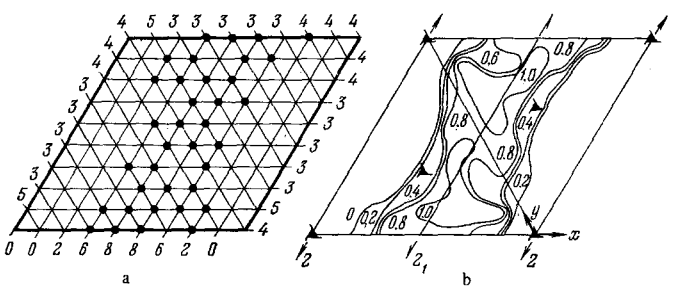

FIG. 21. Algebraic solution for one of the cross-sections of the unit cell of hexagonal catalase (a) (the numerical values of the projections are given at the side; the points correspond to $\rho^c = 1$ and the empty nodes to $\rho^c = 0$; there are five such solutions); and their sum by Eq. (19) as a contour plot (b).

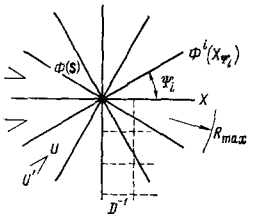

FIG. 22. The transform $\Phi(S)$ and its cross-sections $\Phi^i(X_{\Psi_i})$.

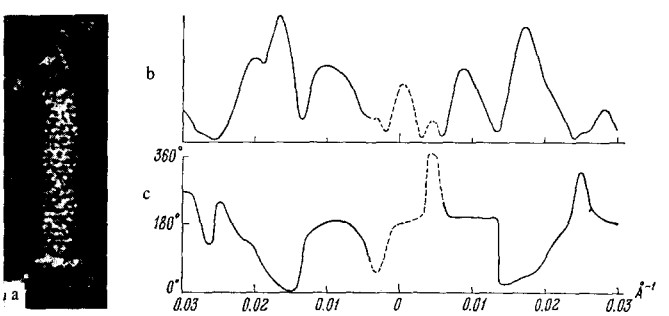

FIG. 23. The tail segment of phage T4 (a); the modulus (b); and the phase (c) of one of the harmonics of its cylindrical transform by (25).

modulus and phase angle for one of the harmonics of the transform of the image of the tail of T4 bacteriophage as obtained thus.[69] The calculations require a rather large amount of machine time. Nevertheless, the method has furnished a number of valuable results that are described below.

g) Synthesis by projecting functions.[52,71] Just like the other methods to be discussed below, this method does not require in its application the transformation (24) into reciprocal space. That is, it is carried out by the direct system of (20). It is intuitively clear that superposition upon one another of projections extended along the direction of projection, as in Fig. 20, should give information on the structure of the sought function. But which ones? Let us examine the two-dimensional case. Let us extend each projection $L^i(x_i)$ along y_i into a two-dimensional "projecting function" $L^i(x_i, y_i)$ (Fig. 24a):

$$L^i(\mathbf{r}) = (1/a)\, L^i(x_i)\, u(y_i), \quad u(y_i) = \begin{cases} 1 \text{ within } b, \\ 0 \text{ outside of } b, \end{cases} \tag{27}$$

where b (>a) is a certain distance. Now let us superpose the p functions $L^i(x_i y_i)$ on one another in the xy plane (Fig. 24b):

$$\sum_{i=1}^{p} L^i(\mathbf{r}) = \Sigma_p(\mathbf{r}). \tag{28}$$

Analogously, a continuous synthesis of a multitude of $L(\psi, \mathbf{r})$ gives

$$\int_0^{\pi} L(\psi, \mathbf{r})\, d\psi = \Sigma(\mathbf{r}). \tag{29}$$

Let us examine how a point, i.e., a δ-function $\delta(\mathbf{r})$, is imaged when we perform the procedure (27)–(29). The projecting function for the point $\delta(\mathbf{r} - 0)$ will be a straight line passing through it (Fig. 24c). Superposition of a discrete multitude of such lines will give a "star" (Fig. 24d), while superposition of a continuous multitude of them is equivalent to rotation of line about the point $\mathbf{r} = 0$, which gives rise to the function $|\mathbf{r}|^{-1} = r^{-1}$ (Fig. 24e). This is the image of $\delta(\mathbf{r})$. Hence, the image of any two-dimensional function $\delta(\mathbf{r})$ will be its convolution with $|\mathbf{r}|^{-1}$:[2)]

$$\int \rho(\mathbf{r}') \frac{1}{|\mathbf{r} - \mathbf{r}'|}\, ds_{\mathbf{r}'} = \widehat{\rho(\mathbf{r})\, |\mathbf{r}|^{-1}} = \Sigma^{\text{two-dim}}(\mathbf{r}). \tag{30}$$

Since $|\mathbf{r}|^{-1}$ becomes infinite at $\mathbf{r} = 0$, convolution with it reproduces the original function $\rho(\mathbf{r})$ well. However, a background arises around each point of $\rho(\mathbf{r})$ that is proportional to $\rho(\mathbf{r})$ at that point, and which declines like $\mathbf{r}^{-1}$. This will give a certain overall background $B(\mathbf{r})$, which declines rapidly as we leave the region of nonzero values of $\rho(\mathbf{r})$. We can find quite analogously that the function $|\mathbf{r}|^{-2}$ plays the role in the three-dimensional case of the function $|\mathbf{r}|^{-1}$:

$$\Sigma^{\text{three-dim}}(\mathbf{r}) = \widehat{\rho(\mathbf{r})\, |\mathbf{r}|^{-2}}. \tag{31}$$

Thus, in both the two- and three-dimensional cases,

$$\Sigma(\mathbf{r}) = \rho(\mathbf{r}) + B(\mathbf{r}) \approx \Sigma_p(\mathbf{r}). \tag{32}$$

For the contrast functions $\rho^c(\mathbf{r})$ of (9), the background is easily distinguished from the image. According to (11) and (13), the mean is

$$\bar{B}_p(\mathbf{r}) = (p - 1)\, \Omega/a^2. \tag{33}$$

Figure 25 gives an example of reconstruction of the object in Fig. 19 by this method. The methods of calculation are described in[72]. Photosummation of the projecting functions is a graphic method.[73] Figure 20 shows the production of such a function, and Fig. 29a shows the formation of the corresponding image for various values of p. One can also reconstruct a complex asymmetric image (see Fig. 29b–e). The structures of a number of phages have been determined by this method (see below).

h) Exact reconstruction in real space. One can directly transform from the function $\Sigma(\mathbf{r})$ of (29) to $\rho(\mathbf{r})$.[74] Let us consider the fact that in the two-dimensional case the functions $|\mathbf{r}|^{-1}$ and $|\mathbf{S}|^{-1}$ are mutually reciprocal transforms:

$$|\mathbf{r}|^{-1} = \mathfrak{F}[|\mathbf{S}|^{-1}]. \tag{34}$$

Now, by forming the autoconvolution $\widetilde{|\mathbf{r}|^{-1}}$ and applying the Laplace operator, we find that

$$\Delta\, \widetilde{|\mathbf{r}|^{-1}} = \Delta \int \frac{ds_{\mathbf{r}'}}{|\mathbf{r}'|\,|\mathbf{r} - \mathbf{r}'|} = \Delta \int |\mathbf{S}|^{-2} \exp(2\pi i \mathbf{r}\mathbf{S})\, ds_{\mathbf{S}} = -(2\pi)^2 \delta(\mathbf{r}). \tag{35}$$

In the synthesis of $\Sigma(\mathbf{r})$ in (30), the point $\delta(\mathbf{r})$ is imaged as $|\mathbf{r}|^{-1}$, and the analytical expression of this imaging is (35). Hence, the integral equation (30) can be solved for $\rho(\mathbf{r})$ by the expression

$$\rho(\mathbf{r}) = -\frac{1}{(2\pi)^2} \Delta \int \frac{\Sigma(\mathbf{r}')}{|\mathbf{r} - \mathbf{r}'|}\, ds_{\mathbf{r}'} = \frac{1}{(2\pi)^2} \int \frac{\Sigma(\mathbf{r}) - \Sigma(\mathbf{r}')}{|\mathbf{r} - \mathbf{r}'|^3}\, ds_{\mathbf{r}'}. \tag{36}$$

By using it, we can reconstruct the exact values of $\rho(\mathbf{r})$

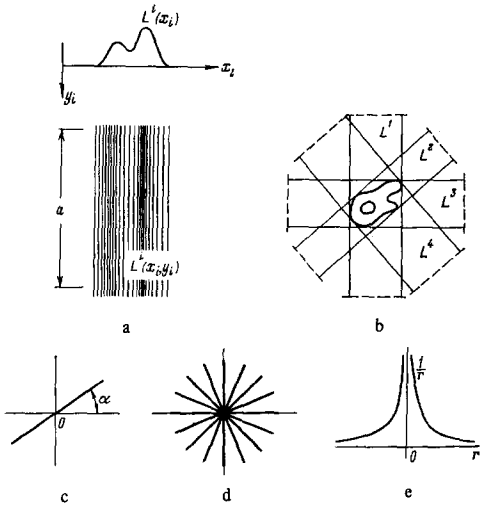

FIG. 24. Formation of a projecting function (a); superposition of these functions (b); the projecting function of a point (c); superposition of these functions (d); and formation of the function $|\mathbf{r}|^{-1}$ (e).

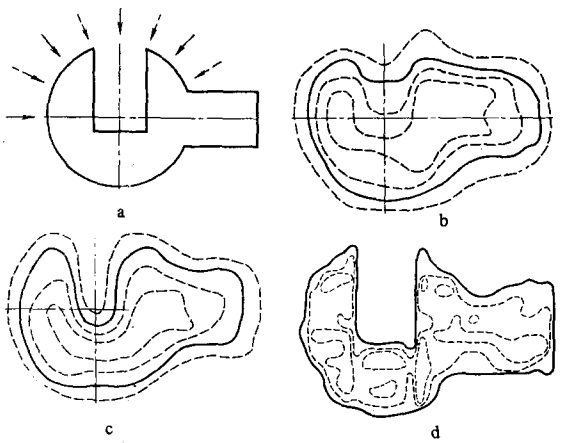

FIG. 25. Reconstruction of the wrench of Fig. 19 (a) from four (b) and eight (c) projections; and reconstruction from eight modified projections by Eq. (46) (d).

from $\Sigma_p(\mathbf{r})$. However, we can also do this without generating $\Sigma_p(\mathbf{r})$, but directly from the set of projections L^i.[55,56,74-78] In order to do this, bearing (21)–(23) in mind, let us write the two-dimensional Fourier transform of the object $\Phi(\mathbf{S})$ in terms of its cross-sections $\Phi(X_\Psi)$ in the form

$$\int_0^\pi \Phi(X_\Psi)\,(2\pi R)\,d\Psi = \Phi(S), \tag{37}$$

where $R = |X_\Psi| = |\mathbf{S}|$.[3)]

The transform of $\Phi(\mathbf{S})$ is $\rho(\mathbf{r})$ (see (23a)). The transform of the product in the integral of (37) corresponds to the convolution of the transform of $\Phi(X_\Psi)$ with $|R|$:

$$\mathcal{L}(X_\Psi) = \widehat{\mathfrak{F}[\Phi(X_\Psi)]}\,\widehat{\mathfrak{F}[|R|]} = \widehat{L(x_\psi)}\,\widehat{K(x)}, \tag{38}$$

Here the first function being convoluted is the original projection $L(x_\psi)$, which we know, and the second function

$$K(x) = \int_{-R_{max}}^{R_{max}} |R| \times \exp(-2\pi i R x)\,dR, \tag{39}$$

is the same for all angles. The product in (37) becomes close to zero when $|\Phi(X_\Psi)| \approx 0$, and these values of $|X_\Psi|_{max} = R_{max}$ are determined by the "dimensions of the inhomogeneities" d of the function $\rho(\mathbf{r})$, such that $R_{max} \gtrsim d^{-1}$. If we take (38) within these limits, we get

$$K(x,\ R_{max}) = R_{max}\,[\sin(2\pi x R_{max})/\pi x] - [\sin^2(\pi x R_{max})/(\pi x)^2]. \tag{40}$$

This function is shown in Fig. 26. Hence, we can calculate the "modified projection" $\mathcal{L}(x_\psi)$ of (38) by[58,74,75]

$$\mathcal{L}(x_\psi) = \int L(x'_\psi)\,K(x'_\psi - x_\psi)\,dx'_\psi. \tag{41}$$

Now we can construct $\rho(\mathbf{r})$ by (23a), with (37)–(40) taken into account, by integrating the functions $L(x_\psi)$ over the angle in real space:

$$\rho(\mathbf{r}) = \int_0^\pi \mathcal{L}(\psi, \mathbf{r})\,d\psi \approx \tag{42a}$$

$$\approx \sum_{i=1}^{p} \mathcal{L}^i(\psi_i, \mathbf{r}). \tag{42b}$$

Here we must extend the $\mathcal{L}(x_\psi)$ along y, as in (27), by transforming them into $\mathcal{L}(\psi, \mathbf{r})$. Thus, by an operation in real space analogous to the projecting-function synthesis of (29), Eqs. (41) and (42) now give an exact reconstruction of $\rho(\mathbf{r})$. In order to do this, we must in advance calculate the convolution of each projection L with the function K.

One can proceed in a different way.[74] Let us represent Eq. (39) in the form

$$K(x) = \frac{1}{2\pi i}\frac{\partial}{\partial x}\int_{-R_{max}}^{R_{max}} \operatorname{sign} R \exp(-2\pi i R x)\,dR \tag{43}$$

and take the limit as $R_{max} \to \infty$. Now, upon starting with (37) and using (21) and (23), we get for $\mathbf{r} = 0$:

$$\rho(0) = -(1/2\pi^2)\int_0^\pi d\psi \int dx_\psi\,[\dot{L}(x_\psi)/x_\psi], \tag{44}$$

or

$$\rho(0) = -(1/2\pi^2)\int_0^\pi d\psi \int dx_\psi\,\{[L(x_\psi) - L'_\psi(0)]/x_\psi^2\}. \tag{45}$$

The principal value of the integral is taken in (44) and (45). In other words, one can calculate $\mathcal{L}(x_\psi)$ by the following formula instead of (41):

$$\mathcal{L}(x_\psi) = -\frac{1}{2\pi^2}\int_0^\infty \frac{L(x'_\psi + x_\psi) + L(x'_\psi - x_\psi) - 2L(x'_\psi)}{(x'_\psi - x_\psi)^2}\,dx'_\psi, \tag{46}$$

and then reconstruct $\rho(\mathbf{r})$ by (42). Figure 27 shows an example of the transformation $L \to \mathcal{L}$ by (46) for one of the projections of the wrench shown in Fig. 19. We see that $\mathcal{L}(x_\psi)$ acquires minima that will truncate the positive background that arises upon integration of the other $\mathcal{L}(x_\psi)$ over the angle ψ. In practice, the integration over the angle in (42a) is replaced by summation by (42b) of a finite number of modified projecting functions $\mathcal{L}^i(\psi_i, \mathbf{r})$. Equation (45) is known as the formula of Radon,[76] who was the first to solve the problem of reconstructing a function from its projections. We note that the maximum contribution to $\rho(\mathbf{r})$ in (42) comes from $\Sigma(\mathbf{r})$ of (39), owing to the presence of x_ψ^2 in the denominator of (45) and (46).

We have given the derivation of Eqs. (42)–(47) in the overall context of reconstruction theory in connection with the Fourier-transformation method and the projecting-function synthesis.[4)] They can also be derived in the theory of generalized functions without transformation into Fourier space by expanding the δ-function into plane waves.[77] Figure 25d gives an example of reconstruction of the already-familiar object of Fig. 19 by Eqs. (42) and (46).

In practice, we possess a finite number p of the projections L^i (which correspond to p cross-sections Φ^i). This restricts the resolution of reconstruction of ρ. One can improve the smoothness of the solutions by interpolating between the projections, either by using reciprocal space or without it.[74]

i) The iteration method. We saw in the last section that accumulation of information at a point $\mathbf{r}$ of a region being reconstructed from the "rays" incident on it, or straight lines from each projection, gives a picture $\Sigma(\mathbf{r})$ that resembles $\rho(\mathbf{r})$. Analogously, one could construct a product function $\Pi(\mathbf{r})$ or a minimum function $M(\mathbf{r})$ of these data accumulated at the point $\mathbf{r}$.[51]

Gordon, Bender, Herman, et al.[65,66,80-82] have treated the possibility of reconstructing $\rho(\mathbf{r})$ by iterations that cause some initial distribution to approach one satisfying the condition that its projections will resemble the set L^i ("the algebraic reconstruction technique", or ART). On a discrete grid, let us assign ρ_{jl} in a zero-

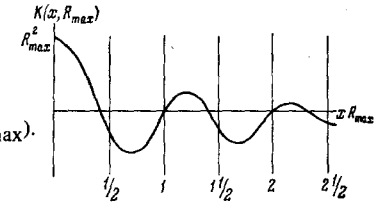

FIG. 26. The function $K(x, R_{max})$.

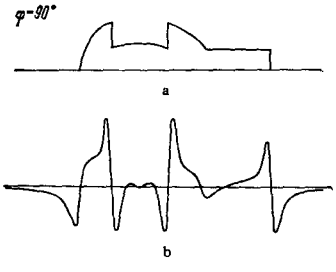

FIG. 27. The original L (a) and its corresponding function $\mathcal{L}$(b) modified by Eq. (46).

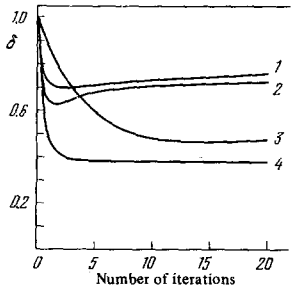

FIG. 28. The relation of δ by Eq. (48) to the number of iterations for different variants of the iteration method (the numbering of the curves is explained in the text).

order approximation to be a uniform distribution of mean values (see (14c))

$$\rho_{jl}^{0} = \bar{\rho} = \Omega/m^2.$$

The projection of the q-th approximation ρ_{jl}^{q} at the angle ψ_i (with (14a) used to account for discreteness) is $L_k^{i,q}$.

The next approximation ρ^{q+1} for each point jl can be obtained by the "multiplication" procedure:

$$\rho_{jl}^{q+1} = (L_k^i / L_k^{i,q})\,\rho_{jl}^{q} \qquad (47a)$$

or by "addition":

$$\rho_{jl}^{q+1} = \max\,[\rho_{jl}^{q} + (L_k^i - L_k^{i,q})/N_{L_k^i};\ 0], \qquad (47b)$$

Here N_{L^i} is the number of points in the projection L_k^i. The latter procedure is less sensitive to errors in measuring the projections. We see that one iteration "adjusts" the projection L_k^q of the previous distribution ρ^q toward L_k^i. One cycle of iterations consists in "running ρ_{ij}^q around all the angles ψ_i." However, proceeding to another angle can impair the results obtained by the iterations at the previous angles. According to[65], the iteration process leads at some $q = Q$ ($Q \approx 10$–20) to getting a certain distribution

$$\rho_{jl}^{Q} \approx \rho_{jl}.$$

Figure 30a gives an example of a reconstruction showing that the obtained images are close to the true function. The reconstruction is carried out here with $m > p$. That is, it does not satisfy the condition of unique solvability. The exact solutions have a "jumpy" ("peppered") character (Fig. 30b), although their sum in the form of (19) is smoother (Fig. 30c). The authors could not state the exact meaning of the obtained functions (47a) and (47b).

Recently Gilbert[79b] found that the iteration process of ART depends on initial application in it of the discretized projections L_k^i of (14a), rather than the true projections of (11). Application of the true projections of (11) initially gives a certain minimum deviation δ of the obtained function from the initial function:

$$\delta = [\sum (\rho_{jl} - \rho_{jl}^{q})^2 / \sum (\rho_{jl} - \bar{\rho})^2]^{1/2}, \qquad (48)$$

The latter can be taken as the "best" reconstruction by the ART, but further iteration impairs the result (Fig. 28, curves 1 and 2). Use of the discretized L_k^i of (14a) initially gives good convergence, but here the true function is reconstructed more poorly (Fig. 28, curve 3).

However, according to[79b], if one starts in the iterations with the true projections L^i of (11), and takes account of the contribution of the rest of the projections as well as the given projection (the SIRT method) by the formula

$$\rho_{jl}^{q+1} = \max\,[\rho_{jl}^{q} + (\sum L^i / \sum l_i) - (\sum L_k^{i,q} / \sum N_{L_k^i}),\ 0] \qquad (49)$$

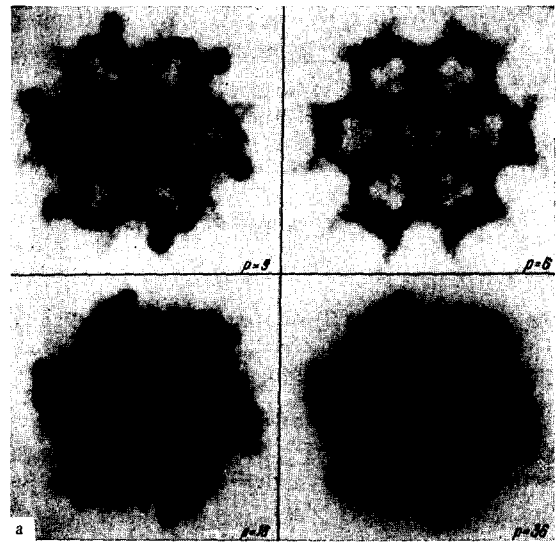

FIG. 29. The function Σ as obtained by photosummation for the pattern in Fig. 20 for p = 6, 9, 18, and 36 (a); examples of asymmetric images (b and c); and their reconstructions for p = 18 (d and e).

FIG. 30. An object and its image as obtained by the iteration method (a) (the number of projections used is indicated); one of the exact solutions of Eq. (17) for p = 8, m = 50 (b); and the average of a set of such solutions (c).

(l_i is the length along y_{ψ_i}), then the process becomes convergent (see Fig. 28, curve 4), and the initial function is reconstructed distinctly enough.

j) Accuracy of reconstruction and resolution.[52,58,64,73,75,81,82] Evidently these characteristics of ρ depend on the number p of existing projections and the experimental errors. The reconstruction is performed on a discrete grid of m × m nodes with a spacing

$a \geq D/m$, where D is the diameter of the function ρ. The condition of algebraic solvability has in general the form $p = m$ (18a), while for contrast functions ρ^C, it has the form $p \lesssim m$ (18b). This means that differing values of ρ_{jk} can be determined with the spacing

$$\lambda = D/p,\ \lambda \leqslant D/p. \tag{50a}$$

These conditions determine the best choice of spacing of the subdivision grid. The function ρ can be characterized by the dimensions d of its inhomogeneities, or the "half-width" of its narrowest peaks. The latter are resolved (a minimum appears between them) if the distance between them amounts to $\approx d$. One can get such a resolution on a discrete grid if the peak covers several nodes, e.g., the linear sequence ... 010100 ... resolves peaks separated by 2a. Thus, in this case,

$$\lambda \gtrsim 2D/p. \tag{50b}$$

We should note that in electron microscopy with negative staining we are dealing with a contrast function ρ^C as in Eq. (9). We must determine its boundary S, which in a discrete representation is marked by a break like ... 000111 ... The criterion (50a) suffices for this. We can also get an estimate of the resolution in the language of reciprocal space. The transform $\Phi = \mathfrak{F}[\rho]$ declines to $|\Phi(\mathbf{S})| \approx 0$ when $|\mathbf{S}| \approx d^{-1}$. On the other hand, in order to reconstruct a ρ with a diameter of D, we must have a grid in reciprocal space with a spacing of D^{-1} (see Fig. 22). The cross-sections of ρ diverge at distances greater than D^{-1} (i.e., they cease to cover the grid) when $\pi d^{-1}/p \approx D^{-1}$. Hence,

$$\lambda \approx \pi D/p. \tag{50c}$$

This is almost the same estimate as (50b). Indeed, the condition for deriving (50c) is too strict, since the values of $|\Phi^i|$ are small at the distance d^{-1}, and they contribute little to the transform $|\Phi|$. We can make a stricter estimate by assigning a concrete form to the inhomogeneities $d(\mathbf{r})$, and thus, to the trend of $\Phi(\mathbf{S})$ in reciprocal space (see Eq. (51) below).

The objects studied in the electron microscopy of biomolecules usually have dimensions $D \approx 200$—400 Å. Given the experimental resolution ≈ 20 Å of stained specimens, the number of projections needed for reconstruction therefore amounts to $p \approx 10$—20.

If the projections L^i have a sharply inhomogeneous angular distribution, e.g., being concentrated in a certain angular range, then the resolution will be anisotropic: greater in the direction perpendicular to the "concentration" direction, and less along that direction.

We can take the correlation functions of the deviation of the reconstructed ρ^* from the true ρ as a measure of the accuracy of reconstruction:

$$R_1 = \Omega^{-1} \int |\rho - \rho^*|\, ds_r,\ R_2 = \int |\rho - \rho^*|^2\, ds_r \Big/ \int \rho^2\, ds_r$$

(one can also use (48) in the discrete representation, in which the integrals are replaced with sums). The quantity R_1 is an analog of the reliability factor in X-ray structural analysis.[83] The "procedural" accuracy depends on the number of projections p and the number of computational operations (interpolation, etc.). The "experimental" accuracy is determined by the mean relative error b of measuring the projections: $\overline{\Delta L} = \overline{|L - L_{exp}|} = b\overline{L}$. One can estimate the procedural accuracy by taking some model function ρ. For a bell-shaped ρ, we get the estimate $R_1 \gtrsim 1/2p$.[58] $R_{exp} \approx b$, whereby we get as a result approximately

$$R_1 \approx b + (1/2p).$$

This quantity is of the order of 10%. In order to estimate R_2, analogously to what is done in crystal-structure analysis,[37,52,84] we can use the completeness theorem

$$\int \rho^2\, ds_r = \int |\Phi|^2\, ds_S.$$

The mean error of the $|\Phi^i|$ corresponding to the L^i is also b. The reconstruction corresponds to using these Φ^i in a "star-shaped" region U of reciprocal space (see Fig. 22), while the region u′ is not used at all. Hence,

$$\int |\rho - \rho^*|^2\, ds_r = \int_U b^2\Phi^2\, ds_S + \int_{U'} \Phi^2\, ds_S. \tag{51}$$

Therefore,

$$R_2 \approx b^2 + f(p),$$

where f is a quantity that is close to zero when (50c) is fulfilled. If $p < m$, then this has an effect in increasing $f(p)$.

4. EXPERIMENTAL STUDIES

Study of a given object encompasses a series of stages. The first is biochemical: to isolate and purify the specimen of interest to us. In preparation for electron microscopy, special procedures are performed of depositing on a substrate, staining, and sometimes crystallization.[4,5] Then one obtains electron micrographs, taking them at different inclination angles if the object is asymmetric.[85] The usual electron-microscopic magnification is of the order of 50,000—100,000. It is very important to select good micrographs, which are then used for the three-dimensional reconstruction. Figure 32 shows an overall diagram of how a study is conducted.

The fundamental process of three-dimensional reconstruction is shown on the left-hand side. After one gets the projections L^i, one can perform the reconstruction either by the Fourier method or by direct methods in real space. The dotted lines indicate procedures that can supplement the reconstruction as taken in the narrow sense of the word. The right-hand side shows the possibility of using X-ray diffraction in combination with electron-microscope data, which we shall treat in more detail below. Now we shall discuss a set of concrete studies.

a) Study of catalase using the method of linear equations of (17). Catalase is an enzyme that catalyzes the decomposition of hydrogen peroxide into water and oxygen. The molecular weight of catalase is about 240,000. It has been shown biochemically that it can be dissociated into two and then four subunits. This protein is easily crystallized to form three- or two-dimensional crystals,[61-63,86-88] and also tubes.[25-27] The hexagonal modification of catalase from beef liver has been studied. Electron-microscopic and X-ray study made it possible to determine the unit-cell dimensions of wet (I—II) and dry (III) crystals given in Table I. There are six molecules per unit cell. The space group of the structure is $P3_121$. The volume Ω_m of the catalase molecule found from density measurements is 300,000 Å^3. Figure 31 shows a catalase crystal, and corresponding micrographs of the structure in state II, which is close to III, in orientations along [10$\bar{1}$0] (c) and [0001] (d) (see Table I). Figure 33a is a contour plot of the values of $L(x, z)$ found from Figs. 31c and d. Owing to the presence of the 3_1 screw axis, this projection is equivalent to three projections, that is, there are three one-dimensional projec-

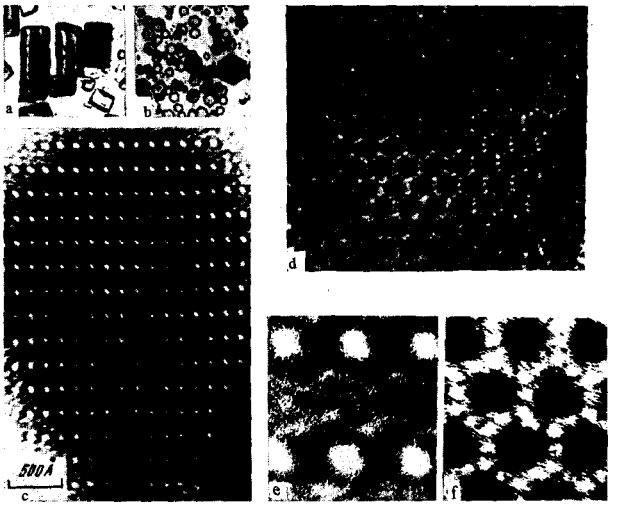

FIG. 31. Crystals of hexagonal catalase in two orientations (in the optical microscope at 200 X magnification (a and b); the corresponding electron micrographs (c and d); and magnified regions of them (e and f).

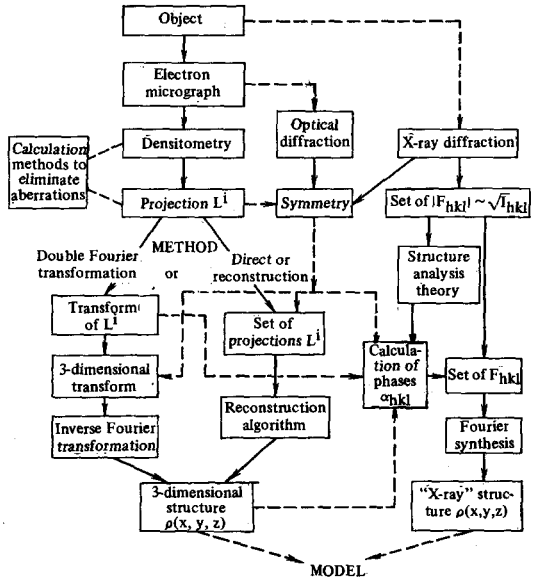

FIG. 32. Block diagram of three-dimensional reconstruction. Left: basic operations of transformation from electron micrographs to ρ, which can be performed by direct reconstruction or by the Fourier method (possible use of optical diffraction is shown; right: combination with the X-ray diffraction method.

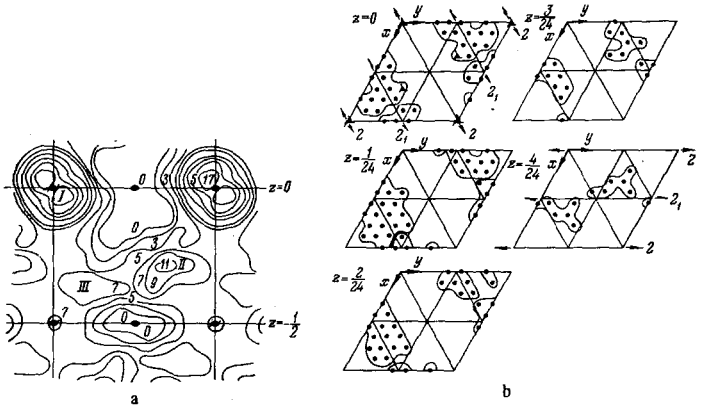

FIG. 33. Contour plot of the projection corresponding to Fig. 31e (the symmetrically independent region) (a); and solutions for five independent cross-sections of catalase (b).

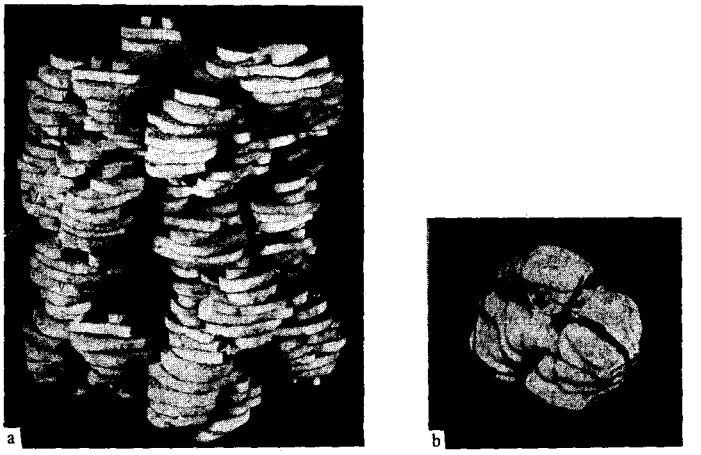

FIG. 34. The structure of crystals of hexagonal catalase (three-dimensional reconstruction) (a); and an individual molecule (b).

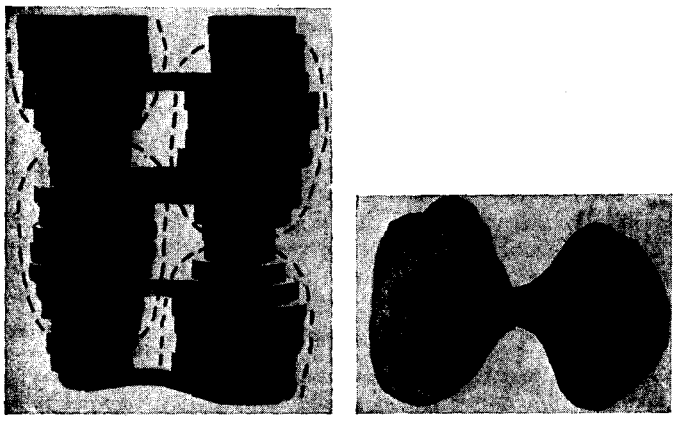

FIG. 35. Reconstruction of an element of the actin filament.

Table I. Parameters of the modifications of hexagonal catalase

Parameters	X-ray diffraction	Electron microscopy	
	Crystal type:		
	Wet (I)	Intermediate (II)	Dry (III)
a, Å	173.3	165—155	130
c, Å	237.4	240—235	200—180
Ω, 10^6 Å^3	6.14	5.5—4.7	2.9—2.6
$x_0 = \Omega_M n/\Omega$	0.30	0.36—0.4	0.67—0.75

tions for each two-dimensional cross-section of $\rho(x, y, z)$ at z = constant. Reconstruction was performed in the proper manner for the contrast function ρ^c of Eq. (9). In accord with (18b), m = 9 was chosen. The interval Δz was taken to be c/24 = 10 Å. That is, four independent cross-sections were reconstructed. A sorting algorithm made it possible to find a set of solutions for each of them. For i > 1, the criterion for selecting the most probable solution was taken to be similarity of the solutions in adjacent sections. This is equivalent to choosing molecules having the least surface. Moreover, the experimental projection along [0001] (Fig. 31d, f) was also taken into account, in that the projection of the found distribution of the protein $\rho(x, y, z)$ in the unit cell must resemble it. Plates of thickness c/24 were prepared from "patterns" like those in Fig. 33b, and superposition of them gave a three-dimensional model of the structure (Fig. 34a).[61] The obtained distribution ρ describes both the packing of molecules in the crystal and their intrinsic structure at a resolution ~ 20—30 Å.

The molecules form an open packing, being seemingly threaded on the 2_1 axis. Their shape manifests clearly the two subunits of molecular weight ~120,000. Examination of the arrangement of subunits and the shape of the molecule as a whole shows that it has the tetrahedral symmetry 222, which agrees with existence of four subunits. The boundary between the smallest subunits of molecular weight 60,000 is marked as well. Figure 34b[63] shows a model of the molecule as averaged over its intrinsic symmetry axes. The dimensions of the molecule along its three axes are about 70, 80, and 95 Å. The coordinates of the center of gravity of the molecule are x = 0.64 ± 0.006, y = 0.14 ± 0.06, z = 0.05 ± 0.03. The subunits of 60,000 molecular weight have dimensions of about 55 Å × 47 Å × 40 Å, and their centers of gravity form a flattened tetrahedron of sides 55, 47, and 35 Å.

Thus, electron microscopy has given a quantitative result which could have been obtained heretofore by X-ray diffraction, even at the low resolution of ~ 20—30 Å, by an incomparably longer path.

The point is that, besides the colossal experimental laboriousness, of X-ray structural analysis of protein crystals, the latter requires in its performance a complex procedure of introducing heavy atoms into the protein and taking diffraction patterns of these isomorphous crystals in order to determine the phases of the reflections.[8-10] However, an undoubted advantage of X-ray structural analysis is the possibility of getting high resolution and analyzing not only the quaternary, but also the tertiary and secondary structure. Nevertheless, electron microscopy can become an important stage even in an X-ray structural analysis, at least at low resolutions, since the calculated distribution $\rho(x, y, z)_{EM}$ can be used to calculate by (21) the phases α_{hkl} of X-ray reflections whose moduli have been determined experimentally.

In order to do this, we must first convince ourselves that ρ_{EM} in the stained crystals studied in the electron microscope and ρ_{XR} in the wet protein crystals resemble one another. We can do this by comparing the amplitudes $|\Phi_{hkl}|$ for the two distributions. Figure 36 shows the optical diffraction pattern of the electron micrograph in Fig. 31d and the corresponding X-ray diffraction pattern. It clearly indicates that the structures are similar, and hence, one can calculate the phases from ρ_{EM}. Such a calculation has been performed under various assumptions, and as a result it has permitted us to construct a Fourier synthesis of the electron density from $|\Phi|_{XR,exp}$.[88] It gave a more detailed picture of the crystal structure and the quaternary structure of the catalase molecule (Fig. 37), which resembles in fundamental features the electron-microscopic model of Fig. 34b.

Thus we see that the single way of studying the structure of protein crystals (X-ray structure analysis with introduction of heavy atoms) can now be supplemented by electron microscopy, and as yet at low resolutions, even replaced by it.

b) Studies by the double Fourier transformation method. A series of studies by DeRosier, Klug, et al. performed by this method has been concerned with structures of cylindrical and also icosahedral symmetry. Asymmetric objects (ribosomes) have also been studied.

Let us discuss the data from study of muscle proteins.[19,89,90] As we know, muscle is built of the fibrous proteins actin and myosin, and their filaments interact with one another and make possible the functioning of the contractile mechanism of muscle. The actin filaments can be isolated separately (Fig. 38a). They have a diameter of about 80 Å, and are made of globular subunits (of molecular weight 45,000) arranged on a double helix having the symmetry s_{13} with c/p = 55 Å. A purified specimen can also be prepared in the form of a "paracrystal" made of these filaments (Fig. 38b). Figure 35 shows a reconstruction of the actin filament that reveals the globular subunits and the bonds between them.[89] Actin filaments isolated directly from muscle and "decorated" with the so-called subfragments of myosin have a more complex structure (Fig. 38c). They have the same symmetry. The subfragment molecule has a thickness of about 45 Å and a length of about 150 Å. The reconstruction is given in Fig. 40a, while Fig. 40b shows a model of such a filament. A fundamental feature is the inclination of the subfragments. This implies a polarity, or "arrowlike" nature of the structure, which makes it possible to concretize the molecular mechanism of muscular contraction.

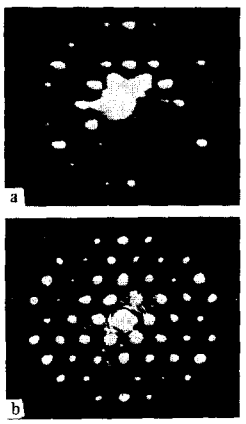

FIG. 36

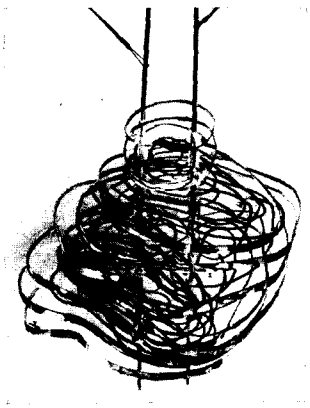

FIG. 37

FIG. 36. Comparison of the X-ray diffraction pattern (hk0 zone) (a); and the optical diffraction pattern (b) of catalase from the micrograph in Fig. 31d.

FIG. 37. Electron density of the catalase molecule at a resolution about 30Å, as found by the right-hand side of the block diagram of Fig. 32.

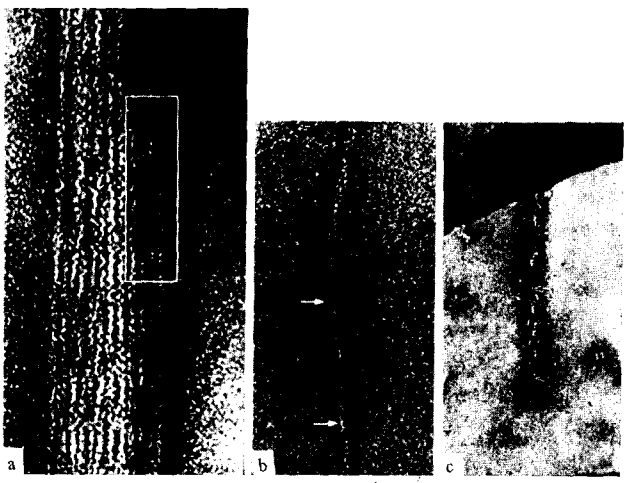

FIG. 38. Electron micrographs of a paracrystal of the muscle protein actin (a); an individual filament of this protein (the arrows indicate the ~715Å period) (b); and a filament with subfragments of myosin added (c).

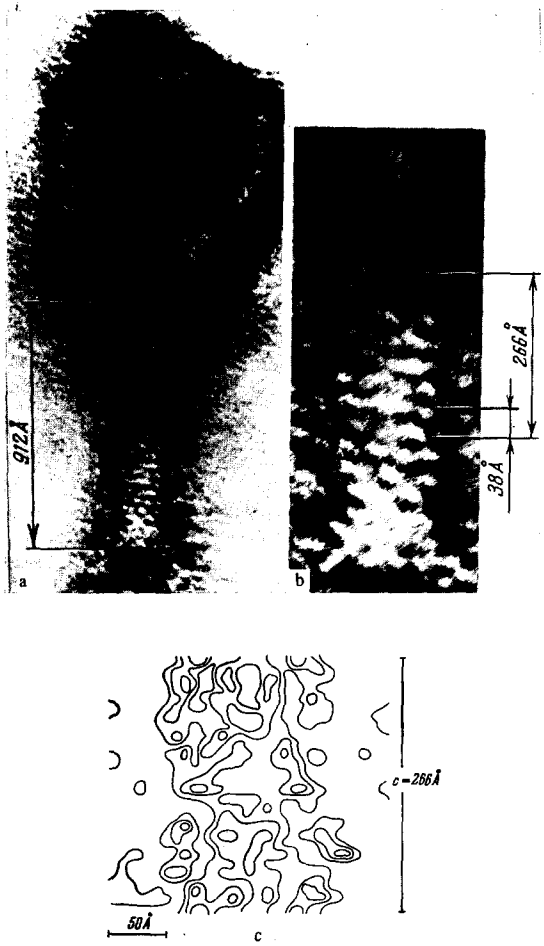

FIG. 39. An electron micrograph of phage T6 (a); a magnified region of the tail (b); and its densitogram (c).

FIG. 40. Reconstruction of an element of the actin filament with subfragments of myosin added (a); and a model of this bihelical filament (b).

The Fourier method has also been used to study spherical viruses of animals and plants.[91,92] These viruses, e.g., herpes, polyoma, poliomyelitis, and turnip yellow mosaic virus, etc., are built of a protein envelope which contains the RNA, or carrier of the genetic information. This RNA enters the host cell and compels the informational-synthetic system of the latter to work at reproducing the virus, rather than the proteins needed by the cell itself.

The closed protein envelope is built of a monomolecular layer of protein morphological units which in a first approximation can be represented by spheres (see Fig. 6d). This envelope is seemingly build of a close-packed layer of these units.[7,17] The most economical principle of construction of an envelope is realized when the ratio of the inner volume to the surface is a maximum. Close packing of morphological units on the surface of a sphere is impossible, but the closest thing to it is an icosahedral packing. The icosahedral point-group symmetry has the symbol 532. That is, it is characterized by presence of six fivefold axes, ten threefold axes, and fifteen twofold axes, while there are correspondingly twice as many points of exit of these axes on the surface. We can see the mutual arrangement of the axes in Fig. 41a. The morphological units at the exit points of the fivefold axes have the coordination number five, while the rest have the coordination number six. Symmetry planes are impossible here, just as in any biological structures made of "left-handed" amino acids.

An individual protein globule (subunit) is always asymmetric. Hence, a morphological protein unit, which is provisionally depicted as a sphere in Figs. 5 and 6, must consist of six protein molecules in the "planar" regions of the envelope and on the edges, i.e., it is a so-called hexamer. At the same time, in order to permit building a closed icosahedral envelope, we must assume that the morphological subunits lying on the fivefold axes and having fivefold coordination are associations of the subunit molecules into pentamers (Fig. 41b). The pentamers and hexamers are distinguishable in electron micrographs (see Fig. 6). The possible number M of morphological units in icosahedral viruses and the number P of protein subunits in the envelopes are determined by the formulas:

$$M = 12_{(\text{pent})} + 10\,(T-1)_{(\text{hex})},\quad P = 60T + 6(M-12),$$

Here the number T can take on certain integer values: T = 1, 3, 4, or 7.[17] Thus, for phage φ, T = 1, i.e., M = 12 and P = 60 (the simplest case). For turnip yellow

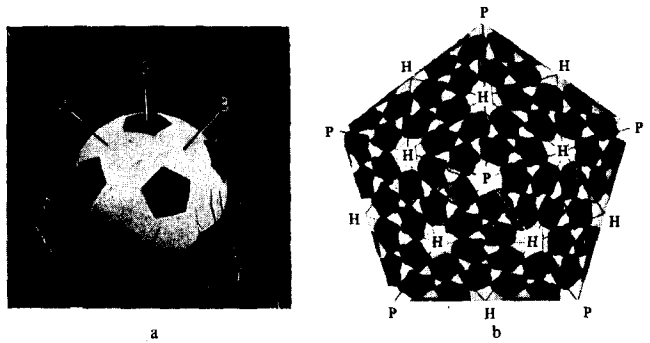

FIG. 41. A soccer ball patterned according to the icosahedral symmetry 532 (a) (the exit points of the corresponding axes are shown); and a diagram of the formation of the morphological units in the envelope of a virus (pentamers P and hexamers H) from asymmetric protein molecules (b).

mosaic virus, T = 3, M = 32, and P = 180, and for herpes (see Fig. 6c) and varicella, T = 16, M = 162, and P = 1500. All of these rules have been established by direct observation and analysis of micrographs of viruses and their empty protein envelopes (lacking RNA). X-ray diffraction analysis also directly confirms the 532 symmetry.

Three-dimensional reconstruction methods have made it possible to refine the idealized models of these viruses.[91,92] The reconstruction was conducted in cylindrical coordinates, and here the most advantageous position of the particle on the substrate had the fivefold axis parallel to the latter. According to (16b), this is equivalent to observing p = 10 projections. Actually, in order to expand the set of ψ in (25a), another particle was selected, also with its fivefold axis parallel to the substrate, but with a different azimuthal orientation. As a result, the effective number p = 20. The orientations were identified from model calculations of the projections[4] (see Fig. 11). The so-called Whittaker-Shannon interpolation[93] was used. This made it possible to arrange the measured data on a regular grid discretized in cylindrical coordinates, as is necessary for the Fourier transformation (Fig. 42). The results of the calculations were averaged over the icosahedral symmetry.

One of the objects was human wart virus (see Fig. 6a). Its diameter is 560 Å, T = 7, M = 72, and P = 420. The result of reconstruction at the relatively low resolution of 60 Å (Fig. 43a) distinctly revealed the icosahedral symmetry and nature of the packing of the particles. At a resolution as good as 40 Å, the hexamers and pentamers appear as "rings" of protein globules.

Tomato bushy stunt virus has a diameter of 330 Å, T = 3, and P = 180. Here the grouping into pentamers and hexamers proves not to be clearly marked, but dimers are more clearly resolved. There are 90 of the latter. Figure 43b shows the reconstruction at a resolution of ~ 30 Å. Blobs of density corresponding to dimers stand out clearly. Some of them lie on the exit points of the twofold axes. These dimers seem more massive, and their radius is greater by 10 Å. The dimer units are grouped in fives around the fivefold axes, but they also enter into sixes around the threefold axes.

Three-dimensional reconstruction of icosahedral viruses is highly promising. Of course, it is more natural here to use their intrinsic symmetry, rather than the cylindrical coordinates in which the calculations were performed.

The double Fourier transformation method has also been used for studying asymmetric particles, the ribosomes.[94] These elongated particles are built like a "mushroom": of a "cap," or so-called 40S subunit, on an ellipsoidal base, or so-called 60S subunit. The height of the particle is about 260 Å, and the "diameter" about 220 Å (see Fig. 9[21-23]).

There is no symmetry in this case, and in order to get a set of projections of a stained specimen, i.e., at different inclinations, a special device was built and mounted in the Philips EM-300 instrument.[85] The number of projections amounted to p = 15. The very laborious calculations resulted in the picture shown in Fig. 44. It corresponds in general features to the known model, but we should consider it as yet only as evidence of the potentialities of application of the method to asymmetric objects.

Ribosomal particles pack into helical "braids" to form a paracrystalline packing in the so-called chromatoid bodies of certain amoebas (Fig. 45a). Several different braids have been found, with the symmetries $s_{12/5}$, $s_{17/5}$, and $s_{19/7}$, with the respective diameters 410,

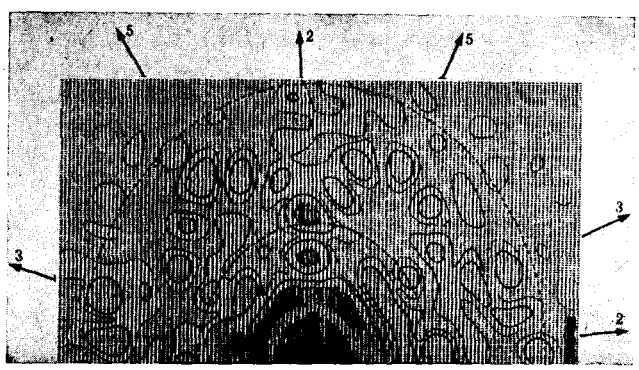

FIG. 42. A region of the two-dimensional Fourier transform of tomato bushy stunt virus (a cross-section perpendicular to the 2 axis) in which values of log |F| are indicated.

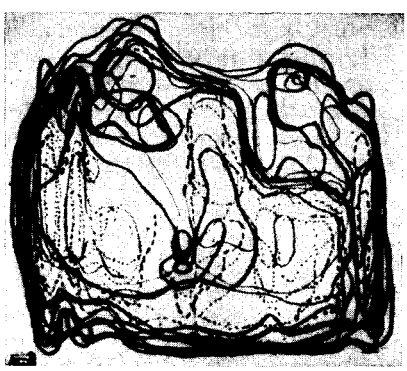

FIG. 44. Reconstruction of a tetramer of ribosomes.

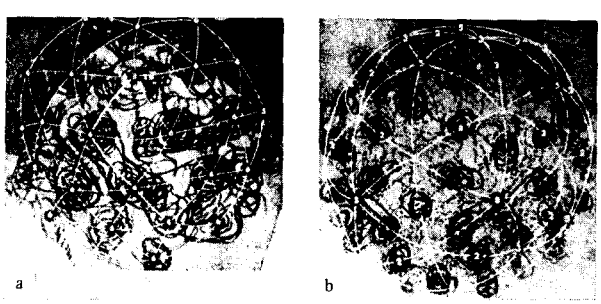

FIG. 43. Reconstructions of the structures of wart virus (a) and tomato bushy stunt virus (b).

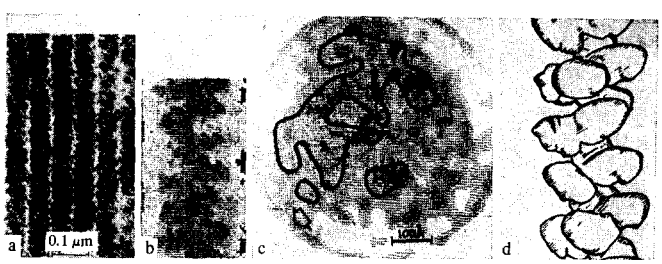

FIG. 45. An electron micrograph of chromatoid braids (a); the density of a braid filtered out of the background on a computer (b); one of the reconstructed cross-sections (c); and a three-dimensional model of a chromatoid braid (d).

500, and 560 Å. A three-dimensional reconstruction was performed by the Fourier method with preliminary mathematical filtering of the image (Fig. 45b). Figure 45c shows one of the cross-sections (perpendicular to the axis of the helix).

The resolution of the reconstructed picture is ~ 50 Å. Figure 45d shows a three-dimensional model of a chromatoid braid. The particles in the packing have a shape similar to that of ribosomes as studied by other methods.[5)]

c) Studies performed by the method of synthesis by projecting functions. The structures of the tail segments of the T-even phages of E. coli B (T2, T6, and DD6) have been studied by this method.[72,97] Phage T4 belonging to the same group has been studied by the double Fourier transformation method,[69] and we shall compare the obtained data here. Figure 39 is a micrograph of the tail of phage T6 and its densitogram. These bacterial viruses belong to the group of complex viruses. Their fundamental morphological components are: the head, which contains the nucleic acid; the tail, which introduces the nucleic acid into the cell being infected; and an apparatus for attaching the tail to the bacterial cell. The tail consists of a hollow cylindrical core of molecular weight 2.3×10^6—3.2×10^6 and a sheath of molecular weight 7.8×10^6—8.0×10^6. The sheath of the tail is the contractile organ, and it can exist either in the contracted state or in the extended state characteristic of the intact particle. The tails of these bacteriophages have helical symmetry.

The parameters p, q, and N of the helix were determined by optical diffraction[98] (Fig. 46a). According to the selection rule (7),[34,36] Bessel functions whose order is a multiple of the order N of the rotation axis of the object participate in producing the reflections in the diffraction pattern. It was found that N = 6. Thus, these structures can be described as piles of disks having sixfold axes (Fig. 20 shows an object of approximately this configuration). The disks lie on one another with a rotation determined by the parameters p and q. These parameters are also determined from the optical diffraction pattern: p/q = 7/2, and the symmetry is $s_{7/2}6$. Thus, the rotation of the elementary disk with respect to the next one is $4\pi/7 \approx 103°$. Every eighth disk is translationally equivalent to the first. That is, it lies exactly under (or over) the latter in the same angular orientation. The elementary grouping is the grouping of smallest volume whose translational repetition can describe the entire object; it contains a certain number of asymmetric groupings in agreement with the order of the group. In line with (16c) and (16d), one projection of the tail (and this means also one of the elementary disk) is equivalent to p = 21 projections, which suffices for reconstruction. Table II gives the diameters of the tail segments, their periods, and certain other source data. Thus, determining the structure of one disk suffices for determining the spatial structure of the tail segment. The thickness of a disk is about 40 Å. Their structure was calculated in four cross-sections separated in height by c/4p, i.e., about 10 Å. From the densitogram in Fig. 39c, $4 \times 7 = 28$ corresponding cross-sections were taken. They could be represented as projection transforms (Eq. (11)) for each of the four sections. Figure 46b shows one of them.

Figure 47 shows the four functions Σ (Eq. (28)) as contour plots of the cross-sections of the elementary disk. Since the outer radius of the phage is known, the value of the edge contour that marks presence of protein in the object is also known. This (or taking account of the volume of the object) makes it possible to select the contour that marks the boundary of the protein.

We can get a model of the elementary disk (Fig. 48a) by extending each section ρ_j by 9.5 Å along the z axis, thereby making disks, and placing these disks on one another. Superposing these disks on one another with a 103° rotation gives the three-dimensional structure (Fig. 48b).

Figure 49 shows models of the tails of the phages T2 and DD6 obtained in the same way. The tail segments have similar structures, but differ only in their dimensions. The diameter of T6 is 170 Å, while the other phages have similar dimensions (see Table II). Two families of helical grooves are observed on the outer surface of the tail segment that seem to form parallelograms on the surface of a cylinder. These are the unit

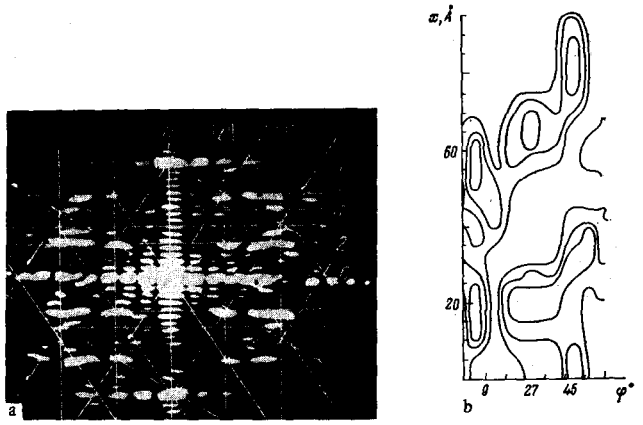

FIG. 46. The optical diffraction pattern of the tail of bacteriophage T6 (a) (the numbers of the layer lines are indicated at the side, and the orders of the Bessel functions of the principal maxima are indicated on the vertical lines); and the projection transform of one of the four independent cross-sections of T6.

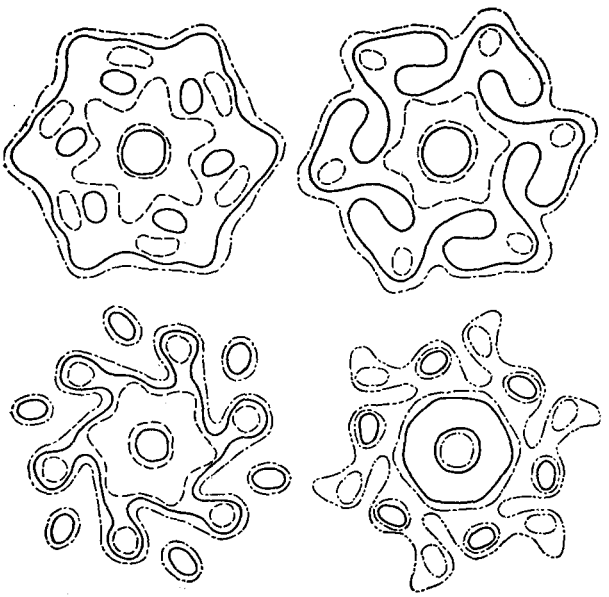

FIG. 47. The function Σ of Eq. (28) for four independent sections of the elementary disk.

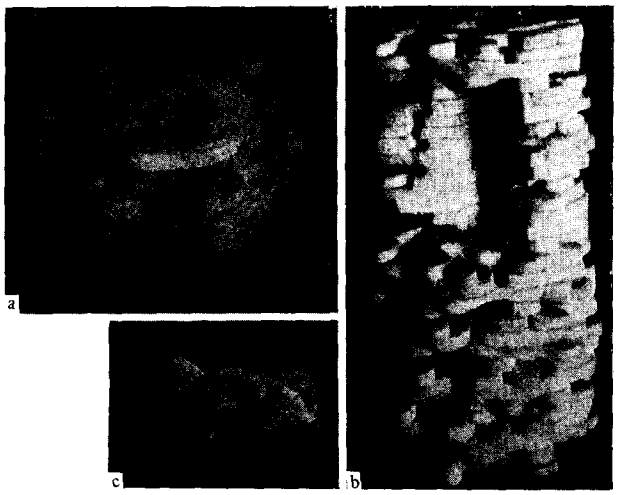

FIG. 48. The elementary disk (a); the three-dimensional structure of the tail of phage T6 (the cutout section shows the axial channel and one of the helical channels) (b); and the structure of the subunits of the sheath (c).

FIG. 49. The three-dimensional structure of the tail segments of phages T2 (a) and DD6 (b).

Table II. Fundamental parameters of the extended tail segments of phages T2, T4, T6, and DD6 of E. coli B

Parameter	T2	T6	DD6	T4
p/q	7/2	7/2	7/2	7/2
N	6	6	6	6
c/p, Å	40	38	41.5	38
Length of tail, A	960	812	996	812
Number of asymmetric units	144	144	144	144
Outer diameter of tail, A	165—170	170	206	240
Diameter of the axial channel of the core, A	20—25	25—30	35—40	30
Outer diameter of the core, A	70—80	85	90—100	100
Diameter of the helical channels, A	20	20—30	30	30
Distance from the axis of the tail to the axial channels, A	40—45	45	60—65	65
$\frac{\Omega}{\mu}$ sheath	1.3	1.5	1.5	
$\frac{\Omega}{\mu}$ core	1.5	1.1—1.4	1.1—1.5	
$\frac{\Omega}{\mu}$ tail segment	1.3	1.3—1.4	1.6	

cells of the so-called radial projection. There are six unit cells about the equator of the model to correspond to the number of asymmetric units in the disks. There is a central cylindrical channel along the axis ($d \approx 30-35$ Å). In addition, six helical channels of somewhat smaller dimensions are found at some distance from the axis of the tail segment (see Table II). Two density maxima are found along the radii of the tail segments. One of them directly abuts the axial channel, and the other is on the periphery of the tail segment. The maxima near the axis correspond to the protein molecules that form the so-called phage core, and the peripheral ones correspond to the sheath. The synthesis allows us to assume that the asymmetric units of the sheath apparently consist of two protein subunits (Fig. 48c). Each of the six peripheral density maxima in the assembled model appears as a "dumbbell" of irregular shape with a volume of about 50,000 Å^3 (see Fig. 48c).

We can conveniently describe the "polypeptide matter" proper of the protein molecules with a quantity numerically equal to the ratio of the volume Ω (in Å^3) to its molecular weight M. This quantity should have the value

$$\Omega/M = m_H/\rho \approx 1,\ 3, \qquad (52)$$

where m_H is the mass of a hydrogen atom, which is 1.65×10^{-24} g; ρ is the density of the protein, which is 1.27×10^{-24} g/Å^3. The value given in (52) is confirmed well by X-ray structural analysis of a number of proteins. Table II gives the corresponding values of Ω/m.

Table II also shows the numerical characteristics of T4 phage, as obtained by DeRosier and Klug[69] by the Fourier method. They are in general similar, apart from the 240-Å diameter of T4, which also deviates from the other electron-microscopic literature data:[6] 2R = 160—180 Å. Apparently we can ascribe this discrepancy to the double Fourier transformation (series termination, and the introduction of a function to smooth the "boundary" of the experimental micrograph).

An estimate of the resolution by Eq. (50a) gives 12 Å. However, micrographs of stained phages have a resolution of ~25 Å from optical diffraction data. We should take the latter quantity to be the resolution of the obtained models.

Thus the reconstruction methods have given direct quantitative information on the three-dimensional structure of the tail segments and on the shape and mutual arrangement of the protein molecules that form them. Of course, this is incomparably more than one could draw from mere examination of micrographs like Figs. 39a and b. In particular, the existence of helical internal channels has been established only by reconstruction.

5. CONCLUSION

We are now at the onset of a new approach in electron microscopy, which has already given a number of substantial results. The theory and algorithms of reconstruction of three-dimensional structure make possible the necessary treatment of the experimental data.

It is interesting to note that the theory of reconstruction of functions from projections and similar algorithms, as we have stated, were developed in a number of other fields. This is how the problem was solved of finding the intensity distribution of radio sources from scanning (i.e., projection) data on this intensity.[56-58] In essence, the same problem exists, but on a macroscopic level, in medical radiography.[53-55] Similar problems are treated in the fields of coding and transfer of images.[59] The problem of visual perception, stereo vision, and creation by the brain of spatial images[99] also resembles the discussed set of problems.

With regard to electron microscopy as such, we should should say that the problems of further study of the three-dimensional structures of biomolecules and their

aggregates are problems of biochemistry and of electron-microscopic experimental technique. The biochemical procedures must permit one to isolate, purify, and prepare the necessary objects. The electron-microscopic technique will develop along the line of improving the methods of mounting, increasing the resolution of the stained objects, and of taking micrographs directly from biological preparations without staining.

In the usual system of the transmission electron microscope, the image is formed according to Eq. (1) from the primary beam by absorption and scattering of its electrons by the specimen. However, one can also use the "dark-field" method, in which the image is formed by the electrons scattered at a certain angle θ.[1,5,100] This method can also be applied to unstained specimens.

The method of the transmission scanning electron microscope proposed by Crewe[101,102] is also highly promising. The well-known method of scanning in reflection ("stereoscan")[103] gives a resolution of the order of 100—200 Å. After overcoming very serious experimental difficulties, Crewe was able to build an instrument in which the diameter of the electron beam at the specimen is 5 Å. Scanning the specimen with such a transmitted electron probe and measuring its intensity (Fig. 50a) with subsequent output on a television screen makes it possible to produce an image. One can show that the optical system of such a microscope is equivalent to the formal-geometric "inverted" system of the ordinary microscope. However, although its resolution is less, it has the advantage of easy analysis of the differential distribution $f(\theta, E)$ of the transmitted electrons with respect to the angle θ and energy E (see Fig. 50a), e.g., measuring the elastic and inelastic components, the pure absorption, etc. Thus one can select favorable systems for detecting heavy atoms, or distinguishing the scattering from the specimen from that of the substrate, etc., from absolute measurements, or, e.g., from the ratio of signals from elastic and of certain inelastic components. As an example, Fig. 50b gives the image of a hemoglobin molecule (unstained).[102] Of course, such an isolated molecule has been deformed in mounting, but the obtained image permits us to discern certain details of its tertiary and quaternary structure. Of course, the problem of three-dimensional reconstruction is also important in the scanning transmission electron microscope, since here also the image is a projection.

Application of high-voltage electron microscopy (up to 1 MeV) will create new possibilities in studying biomolecules.[104]

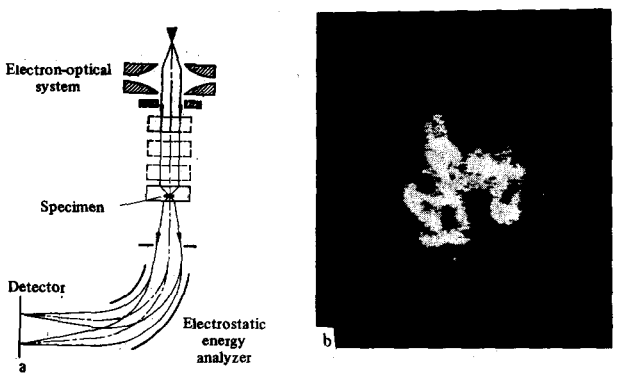

FIG. 50. A fundamental diagram of a transmission scanning electron microscope (a); and an image of a hemoglobin molecule obtained in this microscope (b).

Combination of the ideas of optical diffraction, holographic methods, combination of data from electron microscopy and X-ray diffraction (and all this is just diffraction optics, but with different wavelengths), and widespread use of computers will certainly increase the potentialities for analyzing the structure of biomolecules and of matter in general.

[1)]The theory of reconstruction to be treated below generally does not require (except for specially qualified cases) that the function $\rho(r)$ be positive, but of course, it is applicable to this special case as well.

[2)]See also footnote 3.

[3)]We can give another derivation of Eq. (30) by analogy with (37). According to (22), synthesis by the projecting functions $\Sigma(r)$ of Eq. (29) corresponds in reciprocal space to the expression.

$$\int_0^{\pi} \Phi(x_\Psi)(2\pi)\,d\Psi = \int_0^{\pi} R^{-1}\Phi(x_\Psi)(2\pi R)\,d\Psi,$$

which differs from (37) by the coefficient R^{-1}. The transform of $R^{-1} = |s|^{-1}$ is $|r|^{-1}$ (see 34)), which can be written as a Fourier-Bessel transform of the function R^{-1}: $\int_0^\infty R^{-1} J_n(2\pi rR)(2\pi R)\,dR = \int_0^\infty J_n(2\pi rR)(2\pi)\,dR = r^{-1}$ (in particular also when $n = 0$). Hence the inverse transform of (37') will be the convolution of the inverse transforms of $\Phi(S)$ and R^{-1}. That is, it will be $\widetilde{\rho(r)} * |r|^{-1}$. This gives the conclusion of (30) in the language of reciprocal space.

[4)]Another paper [79a] has recently appeared on this topic, which has been discussed in [58,74,75,78].

[5)]Recently published studies [96] give fuller data.

[1] Z. Leisegang, Electron Microscopy (Russ. transl.), IL, M., 1960.
[2] R. D. Heidenreich, Fundamentals of Transmission Electron Microscopy, N. Y., Interscience, 1964.
[3] I. G. Stoyanova and I. F. Anaskin, Fizicheskie osnovy prosvechivayushcheĭ élektronnoĭ mikroskopii (Physical Fundamentals of Transmission Electron Microscopy), Nauka, M., 1972.
[4] N. A. Kiselev, Élektronnaya mikroskopiya biologicheskikh makromolekul (Electron Microscopy of Biological Macromolecules), Nauka, M., 1965.
[5] D. Kay, Ed., Techniques for Electron Microscopy, Blackwell Scientific Publications, Ltd., Oxford, 1961 (Russ. Transl., Mir, M., 1965).
[6] A. S. Tikhonenko, Ul'trastruktura virusov bakteriĭ (Ultrastructure of Bacterial Viruses), Nauka, M., 1968 (Engl. Transl., Plenum Press, N.Y., 1970).
[7] B. K. Vaĭnshteĭn and N. A. Kiselev, in Virusologiya i immunologiya (Virology and Immunology), Nauka, M., 1964.
[8] M. F. Perutz, Proteins and Nucleic Acids, Amsterdam—London—New York, Elsevier, 1962.
[9] B. K. Vaĭnshteĭn, Usp. Fiz. Nauk 88, 527 (1966) [Sov. Phys.-Uspekhi 9, 251 (1966)].
[10] R. E. Dickerson and I. Geis, Structure and Action of Proteins, N.Y., Harper and Row, 1969.
[11] R. Josephs, J. Mol. Biol. 55, 147 (1971).
[12] A. P. Bois d'Enghien, F. G. Elliott, W. J. Bartels, and E. F. J. van Bruggen, Comp. Biochem. Physiol. B40, 1045 (1971).
[13] A. M. Fiskin, E. F. J. van Bruggen and H. F. Fisher, Biochem. 10, 2396 (1971).
[14] D. J. deRosier and R. M. Oliver, Cold Spring Harbor Symp. Quant. Biol. 36, 199 (1971).
[15] P. Wildy, W. C. Russell and R. W. Horne, Virology 12, 204 (1960).
[16] R. W. Horne, S. Brenner, A. P. Waterson and P. Wildy, J. Mol. Biol. 1, 84 (1959).

[17] D. L. D. Caspar and A. Klug, Cold Spring Harbor Symp. Quant. Biol. **27**, 1 (1962).
[18] R. W. Horne and P. Wildy, Virology **15**, 348 (1961).
[19] B. F. Poglazov, Struktura i funktsii sokratitel'nykh belkov (Structure and Functions of Contractile Proteins), Nauka, M., 1965 (Engl. Transl., Academic Press, N. Y., 1966).
[20] M. F. Moody, Phil. Trans. Roy. Soc. (L.), **B261**, 181 (1971).
[21] H. E. Huxley and G. Zubay, J. Mol. Biol. **2**, 10 (1960).
[22] V. I. Bruskov and N. A. Kiselev, ibid. **37**, 367 (1968).
[23] Y. Nonomura, G. Blolel and D. Sabatini, J. Mol. Biol. **60**, 303 (1971).
[24] A. Klug and J. T. Finch, ibid. **31**, 1 (1968).
[25] B. K. Vaĭnshteĭn, N. A. Kiselev, and I. L. Shpitsberg, Dokl. Akad. Nauk SSSR **167**, 212 (1966).
[26] N. A. Kiselev, C. L. Shpitzberg and B. K. Vaĭnshteĭn, J. Mol. Biol. **25**, 433 (1967).
[27] B. K. Vaĭnshteĭn and N. A. Kiselev, J. Electron. Micr. **16**, 70 (1967).
[28] N. A. Kiselev, F. Ya. Lerner and N. B. Livanova, J. Mol. Biol. **62**, 537 (1971);
[29] C. A. Taylor and H. Lipson, Optical Transforms, G. Bell + Sons, Ltd., London, 1964.
[30] B. K. Vaĭnshteĭn and G. I. Kosourov, Kristallografiya **11**, 921 (1966) [Sov. Phys.-Cryst. **11**, 778 (1967)].
[31] G. I. Kosourov, I. E. Lifshitz, and N. A. Kiselev, ibid. **16**, 813 (1971) [Sov. Phys.-Cryst. **16**, 702 (1972)].
[32] A. Klug and D. J. deRosier, Nature **212**, 29 (1966).
[33] A. Klug, F. H. C. Crick and H. W. Wyckoff, Acta Cryst. **11**, 199 (1958).
[34] W. Cochran, F. H. C. Crick and V. Vand, Acta Cryst. **5**, 581 (1952).
[35] B. K. Vaĭnshteĭn, Kristallografiya **4**, 842 (1959) [Sov. Phys.-Cryst. **4**, 801 (1960)].
[36] B. K. Vaĭnshteĭn, Difraktsiya rentgenovskikh luchei na tsepnykh molekulakh (Diffraction of x-rays by Chain Molecules), AN SSSR, M., 1963 (Engl. Transl., Elsevier, Amsterdam, 1966).
[37] N. A. Kiselev, D. J. deRosier, and A. Klug, J. Mol. Biol. **35**, 561 (1968).
[38] V. N. Zaĭtsev, B. K. Vaĭnshteĭn, and G. I. Kosourov, Kristallografiya **13**, 594 (1968) [Sov. Phys.-Cryst. **13**, 507 (1969)].
[39] B. K. Vaĭnshteĭn, Strukturnaya élektronografiya, AN SSSR, M., 1956 (Engl. Transl., Structure Analysis by Electron Diffraction, Pergamon Press, Oxford, 1964).
[40] P. P. Ferrier, Adv. Opt. and Electron Micr. **3**, 155 (1968).
[41] D. Gabor, Proc. Roy. Soc. **A197**, 545 (1949).
[42] D. Gabor, Proc. Phys. Soc. **B64**, 449 (1951).
[43] G. W. Stroke, New Scientist and Sci. J. **51**, 671 (1971).
[44] M. A. Kronrod, N. S. Merzylakov, and L. I. Yaroslavskiĭ, Zh. Tekh. Fiz. **42**, 414, 419 (1972).
[45] J. Frank, B. Bubler, K. Langer and W. Hoppe, Ber. Bunsenges. **74**, 1105 (1970).
[46] W. Hoppe, Optik **29**, 617 (1969).
[47] W. Hoppe, Acta Cryst. **A26**, 414 (1970).
[48] W. Hoppe, K. Langer, and F. Thon, Optik **30**, 538 (1970).
[49] W. Hoppe, Phil. Trans. Farad. Soc. (L.) **B261**, 71 (1971).
[50] H. P. Erickson and A. Klug, ibid., p. 105.
[51] B. K. Vaĭnshteĭn, Nekotorye voprosy difraktsionnykh metodov (Some Problems of Diffraction Methods), Preprint of the Institute of Crystallography of the Academy of Sciences of the USSR, 1968.
[52] B. K. Vaĭnshteĭn, Kristallografiya **15**, 894 (1970) [Sov. Phys.-Cryst. **15**, 781 (1971)].
[53] D. G. Grant, J. B. Garrison and R. J. Johns, APL Techn. Digest **10**, 9 (1970).
[54] D. E. Kuhl and R. Q. Edwards, Radiology **96**, 563 (1970).
[55] A. M. Cormack, J. Appl. Phys. **34**, 2722 (1963); **35**, 2908 (1964).
[56] R. N. Bracewell, Austr. J. Phys. **9**, 198 (1956).
[57] J. H. Taylor, Astrophys. J. **150**, 421 (1967).
[58] R. N. Bracewell and A. C. Riddle, ibid. p. 427.
[59] W. K. Pratt, J. Kane and M. C. Andreas, Proc. IEEE **57**, 66 (1969).
[60] V. V. Barynin, Kristallografiya **16**, 887 (1971) [Sov. Phys.-Cryst. **16**, 771 (1972)].
[61] B. K. Vaĭnshteĭn, V. V. Barynin, and G. V. Gurskaya, Dokl. Akad. Nauk SSSR **182**, 569 (1968) [Sov. Phys.-Doklady **13**, 838 (1969)].
[62] B. K. Vaĭnshteĭn, V. V. Barynin and G. V. Gurskaya, Acta Cryst. **A25**, p. S181 (1969).
[63] V. V. Barynin and B. K. Vaĭnshteĭn, Kristallografiya **16**, 751 (1971) [Sov. Phys.-Cryst. **16**, 653 (1972)].
[64] R. A. Crowther, D. J. DeRosier, and A. Klug, Proc. Roy. Soc. (London), **A317**, 319 (1970).
[65] R. Gordon, R. Bender and G. T. Herman, J. Theor. Biol. **29**, 471 (1970).
[66] R. Gordon and G. T. Herman, The Center for Theor. Biol. Quart. Bull. **4**, 71 (1971).
[67] S. K. Chang, Communs. Assn. Computing Machinery **14**, 21 (1971).
[68] S. K. Chang and G. L. Shelton, IEEE Trans. on Systems, Man and Cybernetics **1**, 90 (1971).
[69] D. J. deRosier and A. Klug, Nature **217**, 130 (1968).
[70] D. J. deRosier and P. B. Moore, J. Mol. Biol. **52**, 355 (1970).
[71] B. K. Vaĭnshteĭn, Dokl. Akad. Nauk SSSR **196**, 1072 (1971) [Sov. Phys.-Dokl. **16**, 66 (1971)].
[72] A. M. Mikhaĭlov and B. K. Vaĭnshteĭn, Kristallografiya **16**, 505 (1971) [Sov. Phys.-Cryst. **16**, 428 (1971)].
[73] B. K. Vaĭnshteĭn and A. M. Mikhaĭlov, Kristallografiya **17**, 258 (1972) [Sov. Phys.-Cryst. 17, 217 (1972)].
[74] B. K. Vaĭnshteĭn and S. S. Orlov, Kristallografiya **17**, 253 (1972) [Sov. Phys.-Cryst. **17**, 213 (1972)].
[75] G. N. Ramachandran and A. V. Lakshminarayanan, Proc. Nat. Acad. Sci. USA **68**, 2236 (1971).
[76] J. Radon, Ber. Verhandl. Sachs. Ges., Math.-Phys. Kl. **69**, 262 (1917).
[77] I. M. Gel'fand and G. B. Shilov, Obobshchennye funktsii i deĭstviya nad nimi, Fizmatgiz, M., 1958, p. 114 (Engl. Transl., Generalized Functions, Academic Press, N.Y., Vol. 1, 1964).
[78] M. V. Berry and D. F. Gibbs, Proc. Roy. Soc. (L.) **A314**, 143 (1970).
[79] P. F. C. Gilbert, a) ibid. **B182**, 89 (1972); b) J. Theor. Biol. **36**, 105 (1972).
[80] G. Frieder and G. T. Herman, ibid. **33**, 189 (1971).
[81] G. T. Herman and S. Rowland, ibid., p. 213.
[82] R. Bender, S. H. Bellman and R. Gordon, ibid. **29**, 483 (1970).
[83] M. A. Poraĭ-Koshits, Prakticheskiĭ kurs rentgenostrukturnogo analiza (Practical Course of x-ray Structure Analysis), MGU, M., 1960.
[84] B. K. Vaĭnshteĭn, Zh. Eksp. Teor. Fiz. **27**, 44 (1954).
[85] J. Thalen, J. Spoelstra, J. F. L. van Breemen and J. E. Mellema, J. Phys. **E3**, 499 (1970).
[86] B. K. Vaĭnshteĭn, V. V. Barynin, G. V. Gurskaya, and V. Ya. Nikitin, Kristallografiya **12**, 860 (1967) [Sov. Phys.-Cryst. **12**, 750 (1968)].

[87] G. V. Gurskaya, S. Ya. Karpukhina, and G. M. Lobanova, Biofizika **16**, 553 (1971).
[88] G. V. Gurskaya, G. M. Lobanova, and B. K. Vaĭnshteĭn, Kristallografiya **16**, 764 (1971) [Sov. Phys.-Cryst. **16**, 662 (1972)].
[89] P. B. Moore, H. E. Huxley and D. J. deRosier, J. Mol. Biol. **50**, 279 (1970).
[90] M. Watanabe, S. Sasaki and N. Anasawa, JEOL News **9e** (1), 9 (1971).
[91] R. A. Crowther, L. A. Amos, J. T. Finch, D. J. deRosier and A. Klug, Nature **226**, 421 (1970).
[92] R. A. Crowther, Phil. Trans. Roy. Soc. (L.) **B261**, 221 (1971).
[93] E. T. Whittaker, Proc. Roy. Soc. Edinburgh **35**, 181 (1915); C. E. Shannon, Proc. IRE (N.Y.) **37**, 10 (1949) (Russ. Transl., in C. E. Shannon, Raboty po teorii informatsii i kibernetike (Studies on Information Theory and Cybernetics), IL, M., 1963, p. 433).
[94] J. E. Mellema and E. F. J. van Bruggen, Thesis (University of Groningen, 1970), p. 78.
[95] J. A. Lake and H. S. Slayter, Nature **227**, 1032 (1970).
[96] J. A. Lake, J. Mol. Biol. **66**, 255 (1972); J. A. Lake and H. S. Slater, ibid., p. 271.
[97] A. M. Mikhaĭlov and B. K. Vaĭnshteĭn, Dokl. Akad. Nauk SSSR **203**, 955 (1972).
[98] A. M. Mikhaĭlov and N. N. Belyaeva, Molekulyarnaya biologiya **5**, 318 (1971).
[99] D. A. Pollen, J. R. Lee and J. H. Taylor, Science **173**, 74 (1971); J. L. Harris, J. Opt. Soc. Amer. **56**, 569 (1966).
[100] A. K. Kleinschmidt, Phil. Trans. Roy. Soc. (L.) **B261**, 143 (1971).
[101] A. W. Crewe, Phil. Trans. Farad. Soc. (L.) **B261**, 61 (1971).
[102] A. W. Crewe, Scientific American **224** (4), 26 (1971).
[103] G. V. Spivak, G. V. Saparin, and M. V. Bykov, Usp. Fiz. Nauk **99**, 636 (1969) [Sov. Phys.-Uspekhi **12**, 756 (1970)].
[104] V. E. Cosslett, Phil. Trans. Roy. Soc. (L.) **B261**, 35 (1971).

Translated by M. V. King